Software design and implementation of a contactless surface sensing NDE scanning system

by

Alexandru I. Bugar

A Thesis Submitted to the

Graduate Faculty in Partial Fulfillment of the

Requirements for the Degree of

MASTER OF SCIENCE

Department: Electrical Engineering and Computer Engineering
Major: Computer Engineering

Iowa State University
Ames, Iowa
1993

TABLE OF CONTENTS

ACKNOWLEDGMENTS

The author wishes to express his deepest and most sincere appreciation to John Moulder for his guidance and high level technical advice throughout the course of this research. Without his support and professional encouragement this project would not have been possible.

The author would like to thank Satish Udpa for his helpful suggestions and knowledgable advice in writing this thesis.

Thanks are extended to the rest of the committee, Doug Jacobson and Albert Baker, for consenting to serve on the committee.

Special acknowledgments for Norio Nakagawa for helpful advice in various technical problems.

This work was supported by NIST (National Institute of Standards and Technology) at the Center for Nondestructive Evaluation. Grateful acknowledgment is made for their support.

CHAPTER 1. INTRODUCTION

1.1 The Eddy Current Method

Nondestructive evaluation (NDE) is a discipline involved in the inspection and evaluation of the structural integrity and quality of materials without destroying them in the process. NDE is widely used to detect and characterize flaws in engineering parts such as airplane wheels and frames, pressure vessels, bridges and so on. Such defects could result in failure during service and have disastrous consequences.

Over the years, many methods have been developed to interrogate materials, including visual inspection, ultrasonic, radiographic, eddy current, electrical, dye penetrant, and thermographic methods. One of the most commonly used electromagnetic NDE methods is the eddy current method. Eddy current methods are used widely in various industries for the detection and characterization of flaws in conducting, ferromagnetic and nonferromagnetic materials.

The basic components of an eddy current test include: a coil or coils carrying an alternating current, a means of measuring the current or voltage, and the conducting specimen to be tested. The test coil can either be a single coil, or a pair of coils that is part of a balanced bridge circuit. When the coil is excited by an alternating current source and moved over the surface of a specimen, eddy currents are produced in the specimen. The alternating current in the coil produces an alternating magnetic field

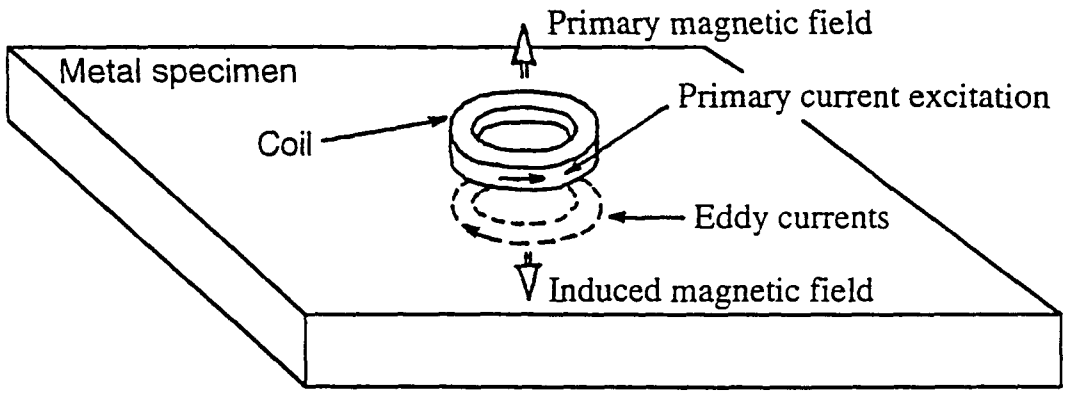

Figure 1.1: The principle of eddy current method

in accordance with the Maxwell-Ampere law. These induced eddy currents in turn, set up a magnetic field in opposition to the primary field in the coil, causing a partial reduction in the field of the coil. This decrease in the magnetic flux linkages associated with the coil causes a change in coil inductance. Accompanying the decrease in the inductance is an increase in resistance of the coil, since the eddy current loss incurred in the specimen has to be met by the source of primary excitation. Eddy current testing involves the measurement of this change in impedance. The principles of this method are illustrated in Figure 1.1. The presence of a flaw in the test material would

change the flow of eddy currents and hence cause a change in the coil impedance. A flaw with its plane perpendicular to the current flow interrupts the normal flow of eddy currents.

When a uniform plane wave is incident on a semi-infinite half plane, the magnetic field within the specimen decays exponentially with depth in the material [1,2]. The depth at which the amplitude of the magnetic field falls to 1/e times the field at the surface is called the skin depth. The value of the skin depth can be determined from Maxwell's equations:

$$\delta = \left(\frac{1}{\pi f \mu \sigma}\right)^{1/2}$$

The skin depth is a function of the excitation frequency f as well as the permeability μ and conductivity σ of the material. Hence the eddy current technique is mainly effective in detecting surface flaws that are not far away from the surface of the material. For detecting subsurface flaws the frequency of excitation has to be low as this would result in a greater skin depth.

With ferromagnetic specimens, the eddy current process is more complicated. Along with the decrease in inductance due to the influence of eddy currents, there is an increase in inductance due to the higher permeability of the material. The latter effect is usually more predominant and hence, when the coil is brought close to such a specimen, the overall inductance of the coil increases along with an increase in its resistance. In practice, however, the change in impedance caused by the presence of a defect in a ferromagnetic specimen is extremely small compared to its quiescent value. Also, variations in permeability throughout specimen can cause spurious signals, confusing the search for flaws. Consequently, eddy current methods are most often used for inspecting non-magnetic materials.

1.2 Factors Affecting Eddy Current Measurements

A major factor that has had a significant impact on NDE is the availability of relatively inexpensive computing power in recent years. The use of computers as a component of an eddy current system and the need for digitizing the eddy current signal can be easily understood if we learn about the complex factors that affect eddy current measurements.

The change in the coil impedance produced by a flaw in general, is very small when compared to the no-flaw impedance of the coil. In addition, the signal includes effects of various factors that can mask the changes due to flaws, making the detection of the defect very difficult sometimes. As presented by R. Halmshaw [3], these variables are:

(1) electrical conductivity of the specimen,

(2) distance between the coil and the specimen called the lift-off,

(3) flaws in the specimen,

(4) magnetic permeability in the case of ferromagnetic specimens,

(5) metallurgical variables in the specimen,

(6) primary coil size (number of turns, diameter, etc),

(7) alternating current frequency,

(8) dimensions of the specimen,

(9) environmental conditions.

One of the major problems in eddy current measurements is to isolate the effects of these variables and correctly interpret the signal. Accurate interpretation of the signal requires testing to be performed under controlled conditions such as fixed environmental conditions and lift-off. It is essential that the lift-off be kept constant

throughout the scan in order to be able to have reasonable quantitative estimates of the flaw size and location.

This thesis investigates the possibility of using inductive sensors for measuring and monitoring lift-off. Controlling lift-off is important not only because it causes significant perturbations in measurements, but also because it allows one to take advantage of one of the major advantages of eddy current testing, namely that physical contact between the test coil and the specimen surface is not necessary. This improves the versatility of the method.

1.3 Aim and Scope of Thesis

Variation in lift-off is an important source of noise in the eddy current inspection of metal parts. This is particularly true in the inspection of parts with complex shapes, where it becomes critical to control the lift-off of the probe very accurately as the scan is performed. In the past, mechanical techniques of spring loading the probe and scanning it in contact with the surface of the part were used. This, however, causes a lot of scanning difficulties and can potentially damage the probe. In order to ensure a reliable and repeatable scan, as well as fast inspection, it is desirable to scan the probe without contacting the surface. But in this case, other problems can occur: small variations in the surface topography can introduce noise, obscuring flaw signals and reducing the probability of detection (POD). To avoid these problems, the possibility of using eddy current sensors to measure the stand-off distance of the probe in order to map the topography of the surface very accurately has been investigated in this thesis. The ultimate objective is to use the sensor output to actively control the height of the probe relative to the specimen surface during

scanning.

Chapter 2 describes the mathematical models employed for characterizing an eddy current test. It then focuses attention on the general problem of calculating the impedance as a function of lift-off of a coil above a semi-infinite conductor. Chapter 3 presents candidate sensors that can be used for measuring lift-off and their characteristics.

Chapter 4 presents results obtained in using the eddy current sensor for inferring surface topography of scanned objects. Chapter 5 introduces the use of image processing techniques for improving sensor resolution. These results show that image processing can also be used with success in processing eddy current 2-D scan data.

Chapter 6 describes the software design and discusses implementation issues involved in controlling the eddy current sensor measurements. Chapter 7 discusses new approaches for scanning strategies in eddy current inspection used for objects with complex geometry and identifies areas for future research activity. Chapter 8 presents a summary of the work involved in this thesis and ends with some concluding remarks.

CHAPTER 2. COMPARISON OF EXPERIMENTAL DATA WITH THEORETICALLY PREDICTED RESULTS

2.1 Measurement Modeling in Quantitative Eddy Current NDE

In order to use a nondestructive test method effectively, it is necessary to fully understand the forward problem describing the field/flaw interaction. Hence there is great interest and need for theoretical models that allow parametric studies relating measurement conditions to signal output. Modeling involves the solution of partial differential equations governing the underlying physical phenomena. A measurement model takes the excitation source as the input and predicts the transducer response by solving the underlying partial differential equations. Analytical, numerical and sometimes hybrid (mixed) methods are available for solving these equations.

2.1.1 Analytical Solutions for Simple Geometries

Much of eddy current nondestructive inspection is based on the principle that the presence of near-surface flaws affects the pattern of the eddy currents induced within the metal specimen. These currents are induced by the application of a time-varying current close to the specimen and are concentrated near the surface due to the "skin effect". Flaw detection is therefore mostly limited to surface-breaking cracks and sub-surface cracks that are within one or two skin depths.

Modeling of this inspection technique involves the solution of Maxwell's equations for geometries of different complexities. Neglecting the displacement current, the governing equation describing the eddy current phenomena can be derived from Maxwell's equations [4]

$$\nabla \times (\frac{1}{\mu} \nabla \times \mathbf{A}) = j\omega\sigma\mathbf{A} - \mathbf{J_s} \tag{2.1}$$

where $\mathbf{A}$ represents the magnetic vector potential, $\mathbf{J_s}$ is the source current density and $j\omega\sigma\mathbf{A}$ is the induced eddy current density.

The exact solution of equation (2.1) can be obtained only for very simple geometries. Several exact and approximate solutions to eddy current problems do exist for axisymmetric and two-dimensional cases. Within the context of eddy current techniques the contributions of Burrows [5], Dodd and Deeds [6], and Auld et al. [7] are relevant. The Dodd and Deeds model will be presented in detail later in this chapter.

Another simple class of eddy current problems is that in which the external magnetic field is uniform and uniaxial in suitable coordinates. The geometry is applicable, for example, in the case of eddy currents in a metal bar or plate within a long solenoid carrying an AC current. The use of uniform field eddy current probes for quantitative NDE is also possible [8,9].

The reduction to an effectively two-dimensional geometry and a scalar variable brings some simple geometries within the scope of exact analytical techniques. The general problem of calculating the impedance of a circular coil with a rectangular cross-section above a semi-infinite conductor is well known [6]. A result for a rectangular cross-section bar is also available from French [10]. Kahn et al. [11] have derived solutions for 90° and 360° corners. Various cylindrical geometries have also been considered by Lawrenson and Ralph [12] and by Bird [13].

2.1.2 Numerical Models

The inadequacy of analytical models for handling complex geometries, such as those relevant to NDE problems, and the increasingly high speed computational power available have led to the use of numerical models. These models are flexible and capable of taking into account complex defect geometries and nonlinearities in the material properties.

Numerical techniques for modeling eddy current phenomena include: finite-difference, finite-element and boundary element methods.

The volume integral method of eddy current modeling represents a flaw in metal as a set of electric dipoles located within volume elements or cells defining the flaw volume. The basis of the method is the Green's tensor for an electric dipole in a half-space so that it is necessary only to discretize the flaw volume; given the dipole distribution, impedance changes may be computed. The method was introduced by Dunbar [14,15]. A similar approach was presented by Muller and Knoblauch in [16].

The finite element method consists in solving the governing equation (2.1) by using a variational formulation. The usual procedure is to determine an energy functional, discretize the region of interest into triangular elements, minimize the functional and solve the resulting matrix equation. The method was introduced in the area of NDE by Lord and was first used for modeling active leakage fields in ferromagnetic samples by Lord and Hwang [17,18]. Significant results were obtained by Yen [19], and Udpa and Lord [20] in developing a two-dimensional model for studying residual leakage fields. Lord and Palanisamy developed a two dimensional axisymmetric finite element model and later extended the model to describe quasistatic eddy current phenomena [21,22]. Lord and Ida [23,24] developed a three dimensional finite

element model for eddy current and magnetostatic NDE problems.

Beissner showed that it is possible to model the interaction of eddy currents with material flaws by using the boundary integral form of Maxwell's equations. He has laid the groundwork for a class of eddy current NDE models for surface-breaking flaws [25]. The general idea is to provide a theoretical and computational framework for the efficient, approximate treatment of three-dimensional flaws in the presence of an eddy current probe of arbitrary configuration. To do this, he developed a boundary integral equation for the magnetic scalar potential on the surface of a conductor of arbitrary shape and then applied the boundary element technique [26] to determine the solution.

In practice, however, three-dimensional modeling of realistic flaw geometries places severe demands on computer memory, and implementation of such accurate models is therefore limited to users with access to a large computer system. In some applications, such as studies of the probability of flaw detection [27,28], large numbers of calculations are needed as a function of probe position, and the computer time needed to generate the required data presents an additional practical difficulty. At the other extreme, there are analytical or semianalytical methods that are easily adapted even to microcomputer applications, but these models are limited by the assumption of simple probe/flaw geometries or other restrictions.

2.2 Dodd and Deeds Analytical Model for Calculating the Impedance of a Coil above a Semi-Infinite Conductor

In practice, the impedance of the test coil is not only modified by flaws in the specimen, but also by other variables. The most important of these are:

* lift-off variations

* local variations of magnetic permeabitity and electric conductivity.

In what follows, we will take into consideration changes in probe impedance produced only by lift-off motion perpendicular to the metal sample.

The general problem of calculating the impedance of a circular coil with rectangular cross-section, above a semi-infinite conductor has been solved analytically by Dodd and Deeds [6] using a vector potential approach. The geometry considered is illustrated in Figure 2.1, which shows an air core coil of thickness t, width Δr, and mean radius $\bar{r}$ located at a distance h above an infinite plane of conductivity σ and permeability μ.

We use the notation of Bahr and Cooley [29] and normalize all dimensional quantities by dividing by $\bar{r}$. For a coil of N turns operating at an angular frequency ω, the relevant analytical expression of the coil impedance at normalized height h is [6]:

$$Z_{TP} = j\frac{\pi \bar{r} N^2}{t \cdot \Delta r^2} \cdot \frac{2}{\sigma \delta^2} \cdot I_{TP}(h) \tag{2.2}$$

where the probe current is given by

$$I_{TP}(h) = \int_0^\infty \frac{I^2(\alpha \cdot \Delta r)}{\alpha^5} \{2t + \frac{1}{\alpha}[2(e^{-\alpha t} - 1) + e^{-2\alpha h}(e^{-\alpha t} - 1)^2 \left(\frac{\alpha - \alpha_1}{\alpha + \alpha_1}\right)]\} d\alpha \tag{2.3}$$

with

$$I(\alpha \cdot \Delta r) = \int_{\alpha(1-\Delta r/2)}^{\alpha(1+\Delta r/2)} u J_1(u) du \tag{2.4}$$

J_1 = a Bessel function of first kind and first order

and

$$\alpha_1 = \sqrt{\alpha^2 + j2(\bar{r}/\delta)^2} \tag{2.5}$$

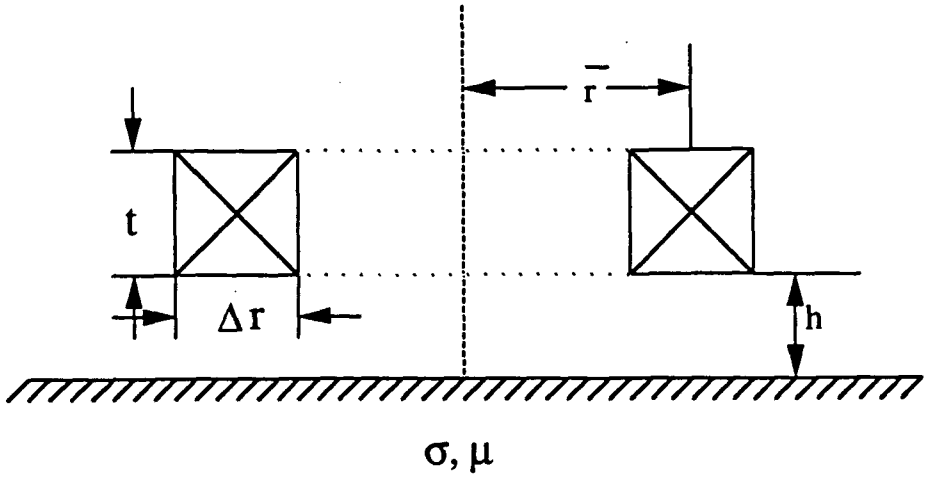

Figure 2.1: Coil geometry for lift-off calculations.

In the expressions above, $j = \sqrt{-1}$, α and u are variables of integration and δ is the electromagnetic skin depth (mentioned in chapter 1).

This method of calculating the coil impedance is accurate except for a few assumptions. As mentioned by Dodd and Deeds [6], the probable sources of errors due to these assumptions include:

1. Axial Symmetry

Coils that have perfect axial symmetry cannot easily be wound. The error will vary with the winding technique and will decrease as the number of turns N on the

coil and the coil-to-conductor spacing increases. Dodd and Deeds [6] showed that for a typical coil, the error should be less than 0.01%.

2. Current Sheet Approximation

This error occurs because a current sheet is assumed in the model. In reality coils are wound with round, insulated wire. For a typical coil [6] with 100 turns, the change in inductance due to this approximation is typically about 0.19%.

3. High-Frequency Effects

These are the most important sources of error in this model. As the frequency increases, the current density ceases to be uniformly distributed over the cross section of the wire, but becomes concentrated near the surface. The resistance of the coil increases, and the inductance decreases. The current is capacitively coupled between the turns in the coil, tending to flow across the loops of wire. The resulting effect is an increase of the interwinding capacitance. Error due to cable capacitance is another consequence of high-frequency effects.

2.3 Comparison of Experimental Results to Dodd and Deeds Theoretical Predictions

2.3.1 Experiment

All impedance measurements were taken with an HP 4194A impedance analyzer, which is capable of measuring complex impedances at frequencies between 10^2 and 10^8 Hz. The coil and its associated cable were connected to the impedance analyzer and the coil was mounted in a fixture over the specimen to permit placing the coil on the surface in a reproducible manner. Measurements of the coil impedance were obtained by modifying the lift-off distance in the Z direction in increments of 0.25 mm.

The specimen was an Al 6061 sample. In order to ensure proper comparison with analytical results, the conductivity of the sample was measured and found to be $\sigma = 2.497 \times 10^7$ S/m. The relative permeability is assumed to be 1 since the specimen is nonferromagnetic.

For the purpose of this experiment, two different absolute air-core coils (probe L and probe A) were employed. Since the results obtained are substantially similar, only measurement results obtained with probe L are given. Table 2.1 provides a few details relating to probe L.

Measurements of lift-off response for eddy current probe L were performed for a lift-off distance ranging from 0 to 4 mm. Table 2.2 shows the experimental data obtained for two frequencies: 500 kHz and 200 kHz. Since the resistive component of the impedance is very small (less than 10% of the inductive reactance) only the reactive component was measured.

Figure 2.2 shows a graphical view of the relationship between the absolute value of imaginary impedance and changes in lift-off, when the excitation frequency is 500 kHz. The second graph in Figure 2.2 illustrates the sensitivity of the probe (dX/dh) to lift-off. It can be observed that the probe sensitivity is very high at lift-off values below 2 mm.

2.3.2 Comparison with Theoretical Predictions

Relations (2.2) and (2.3) of Dodd and Deeds analytical model, presented in Section 2.2, have been implemented in a computer program developed at Stanford [30]. This program calculates first, the integral $I_{TP}(h)$ using Simpson's rule as a function of h, t, $\bar{r}$, Δr and δ, and also the first order Bessel function using polynomial approx-

Table 2.1: Coil and measurement parameters for probe L

	Probe L
Number of turns	235
Inner radius (mm)	0.535
Outer radius (mm)	1.31
Height (mm)	2.93
Internal lift-off	0.56
Inductance in air (μ H)	37.84
Resonant frequency (Mhz)	3.89

Table 2.2: Measurement data

h (mm)	X (ohm) at 500kHz	X (ohm) at 200kHz	h (mm) mid-point	dX/dh at 500kHz	dX/dh at 200 kHz
0	114.491	45.5828			
0.25	115.834	46.0578	0.125	5.372	1.9
0.5	116.689	46.3643	0.375	3.42	1.226
0.75	117.266	46.5708	0.625	2.308	0.826
1	117.645	46.7085	0.875	1.516	0.5508
1.25	117.914	46.8081	1.125	1.076	0.3984
1.5	118.107	46.8793	1.375	0.772	0.2848
1.75	118.253	46.9338	1.625	0.584	0.218
2	118.363	46.9738	1.875	0.44	0.16
2.25	118.449	47.0061	2.125	0.344	0.1292
2.5	118.515	47.0312	2.375	0.264	0.1004
2.75	118.57	47.0515	2.625	0.22	0.0812
3	118.61	47.0674	2.875	0.16	0.0636
3.25	118.648	47.0808	3.125	0.152	0.0536
3.5	118.675	47.0914	3.375	0.108	0.0424

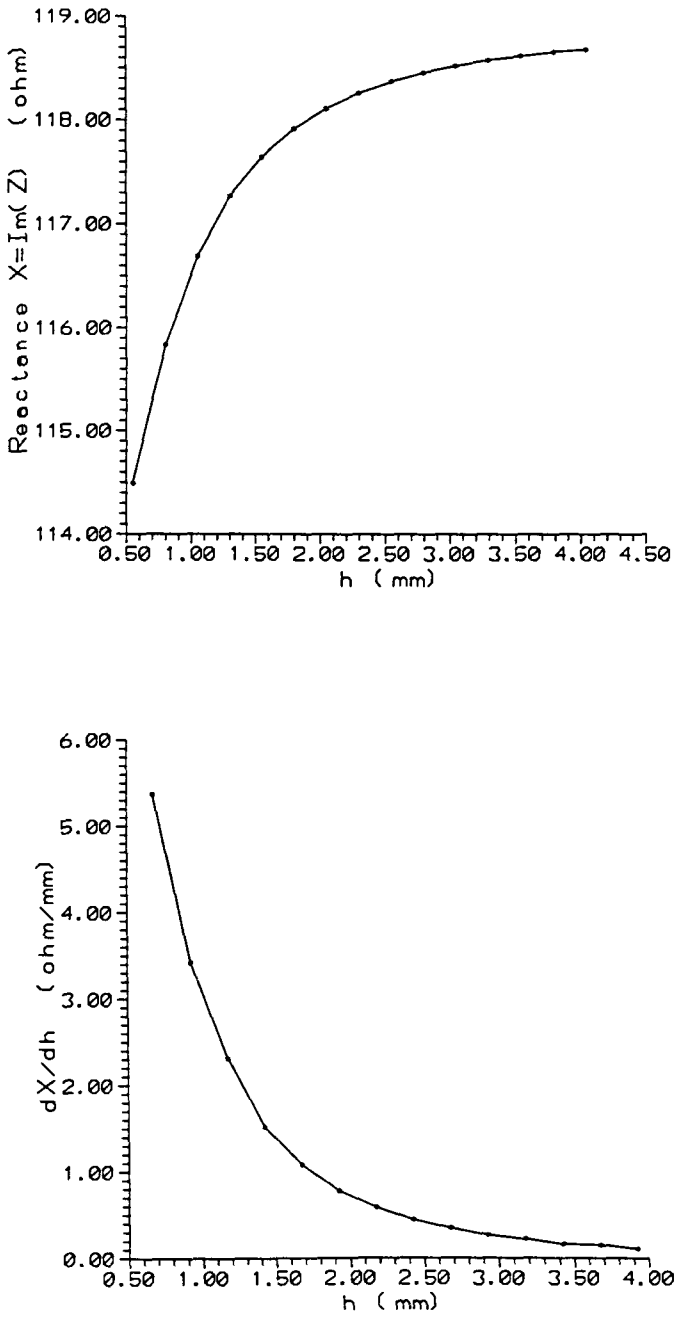

Figure 2.2: Reactance behavior to lift-off changes at 500 kHz

imation techniques. The final output gives the values of the absolute (imaginary) impedance Z_{TP} at different lift-off values. These impedance values and also the lift-off distance values have been referenced relative to the rest position (position when probe is in contact with the sample).

Figure 2.3 shows the reference impedance values that have been calculated for two frequencies plotted on the same graph. The corresponding measured values are also given. It can be observed that measurements of lift-off signals obtained with the air-core probe were found to be in good agreement with the lift-off response calculated from the theory of Dodd and Deeds. Agreement at 200 kHz is very good; the small difference at 500 kHz can be due to the high-frequency effect described in Section 2.2.. Another known source of error is the uncertainty in knowledge of the internal lift-off of the probe (a value determined from radiographs of the probe). It can be shown if the internal lift-off is assumed to be 0.62 mm instead of the manufacturer's specified value of 0.56 mm that is used in calculations, the agreement improves significantly.

The good agreement indicates the need for accurate quantitative measurements. The need for an impedance analyzer and precisely wound air-core coils is also obvious. Greater precision in the manufacture and calibration of commercial eddy current probes is necessary before they can be used with confidence as inductive lift-off sensors in high accuracy applications.

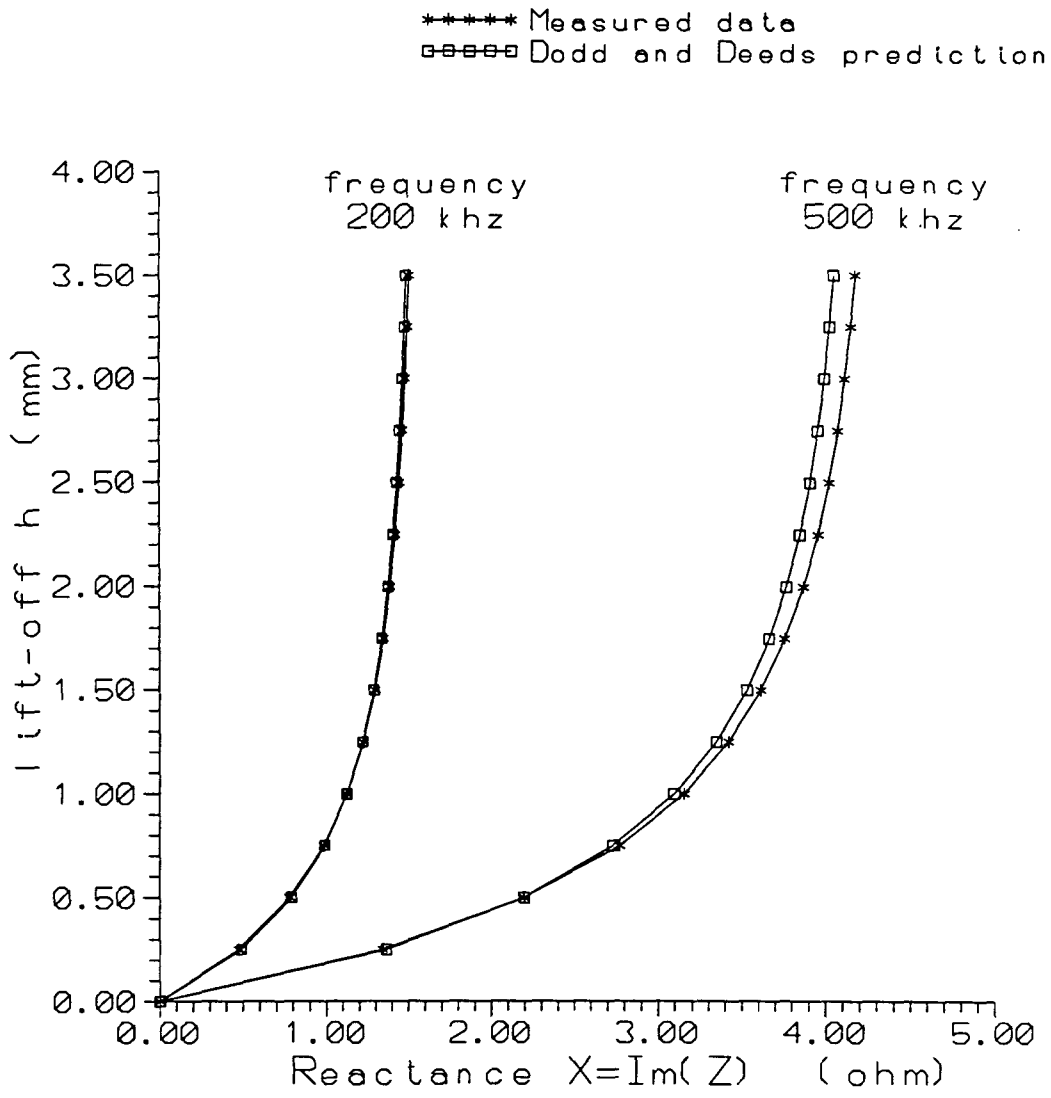

Figure 2.3: Agreement between measured data and Dodd and Deeds theoretical predictions at two operating frequencies

CHAPTER 3. INDUCTIVE SENSORS FOR MEASURING AND CONTROLLING PROBE LIFT-OFF

3.1 Overview

The objective of this research is to develop inductive sensors and scanning strategies to actively measure and control the lift-off of eddy current probes during automated scans of objects with complex geometry. To achieve this goal, an investigation of different eddy current probes was conducted in order to obtain optimal sensor responses. As experiments show, absolute ferrite-core probes give the best results in monitoring lift-off. An analysis of three absolute ferrite-core probes used as inductive sensors is presented in the next few sections.

Other possible approaches that can give good results in NDE and robotic sensing are:

* capacitive sensors [31], which can be used not only to measure the proximity of a metallic object (as inductive sensors can), but also the proximity of a nonmetallic object.

* differential probes [32], which are often used in industry because they are much less sensitive to lift-off noise than conventional absolute probes. As sensors they are used in measuring the tilt of the probe.

* arrays of inductive or capacitive sensors [33,31], which, by using integrated

circuit techniques, can be manufactured into very compact combinations of inductive and capacitive sensor arrays. Such hybrid array systems clearly have the capability of rapidly providing very selective information about both the proximity and the material properties of the object.

In order to improve performance, development of more complex sensors, such as arrays of inductive or capacitive sensors might be considered for future work.

3.2 Sensor Characterization

In order to choose an inductive sensor with high sensitivity, the responses of three absolute eddy current probes were evaluated. They were: a 500-kHz, a 1-MHz and a 2-MHz probe. The frequency values correspond to the nominal operating frequencies. These values could be important when using conventional eddy current measurement systems, but not when a precision impedance analyzer that can measure probe impedance over a broad frequency range is used. To achieve such broad frequency range of operation, impedance analyzers are equipped with an autobalance bridge circuit in the measurement section.

All three probes selected as sensor candidates employ circular ferrite-cored coils, which have the advantage of providing stronger signal amplification relative to air-core probes. We do not have an analytical model for ferrite-core coils. Nevertheless, we could extend Dodd and Deeds theory by adding a circuit model that simulates the strong resonance effect.

One way of characterizing these probes is to obtain their frequency responses in terms of inductive reactance. Figure 3.1 shows the frequency dependence curves plotted by the impedance analyzer. The parameter of interest is the resonant fre-

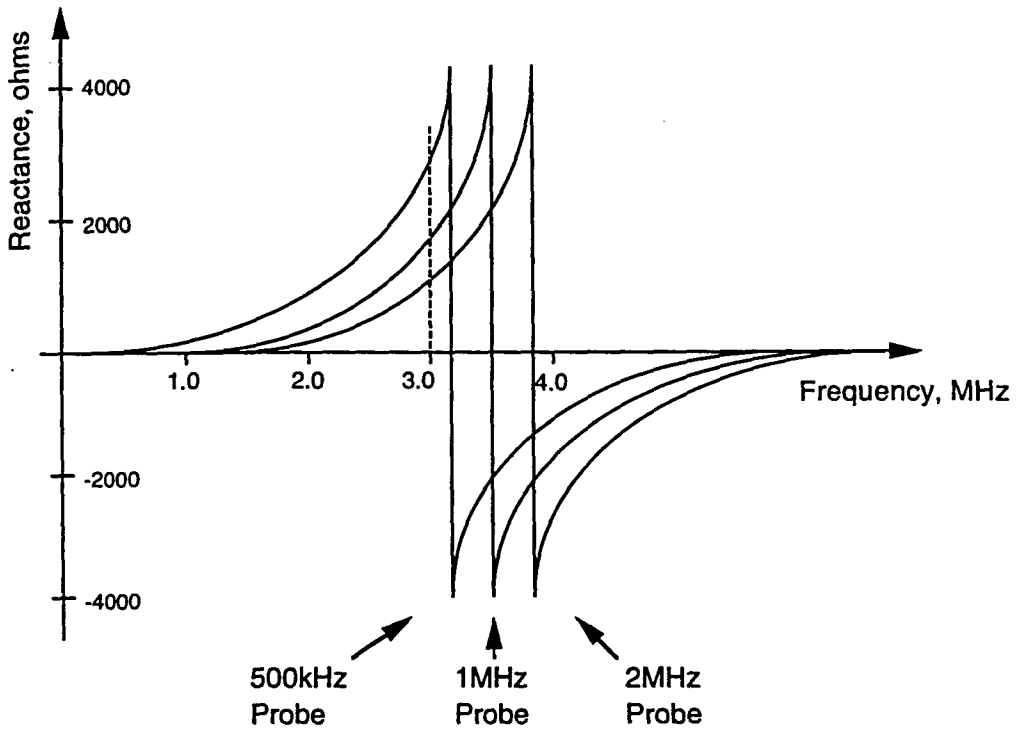

Figure 3.1: The frequency responses for the three absolute probes

quency, which is located close to 3 MHz for all three probes. These resonance curves will be used for analyzing different sensor effects later in this chapter.

3.3 Factors Affecting Inductive Sensors

3.3.1 Operating Frequency

The electromagnetic field frequency range is usually divided into: low frequency, intermediate frequency, and high frequency domains. Eddy current techniques fall in the intermediate frequency or quasi-static domain, where diffusion equations are

applicable. This domain usually includes frequencies from 0.5 kHz up to several MHz. For inductive sensor purposes, the operational frequency can be as high as the resonant frequency of the coil, which is usually above 3 MHz. Experiments show that the use of frequencies very close to resonance give the best results in terms of lift-off discrimination.

The three selected probes were tested in lift-off measurements for different operating frequencies. The frequency range of interest was established between 0.5 MHz and 3 MHz for a test specimen made of Al 6061. Figure 3.1 shows that 3 MHz is still below the resonant frequency of all three probes. Figure 3.2 shows the lift-off signal for one of the three probes (the 500 kHz probe) for five different frequency values. Although each of the five graphs has a different reactance range, it can be observed that the best lift-off discrimination was obtained at the highest frequency (3 MHz). For the other two probes a similar result was obtained.

Therefore, it can be concluded that as we move closer to the resonant frequency, better lift-off discrimination for the inductive sensor is obtained. Again, this is an effect caused by the strong signal amplification due to the resonance of the ferrite-core coil. A word of caution is, however, in order. The curves from Figure 3.1 were obtained with the probe in contact with the sample (zero lift-off distance). If the lift-off increases, there is a slight decrease in the resonant frequency value. This means that the sensor operating frequency should not be set too close to the resonant frequency.

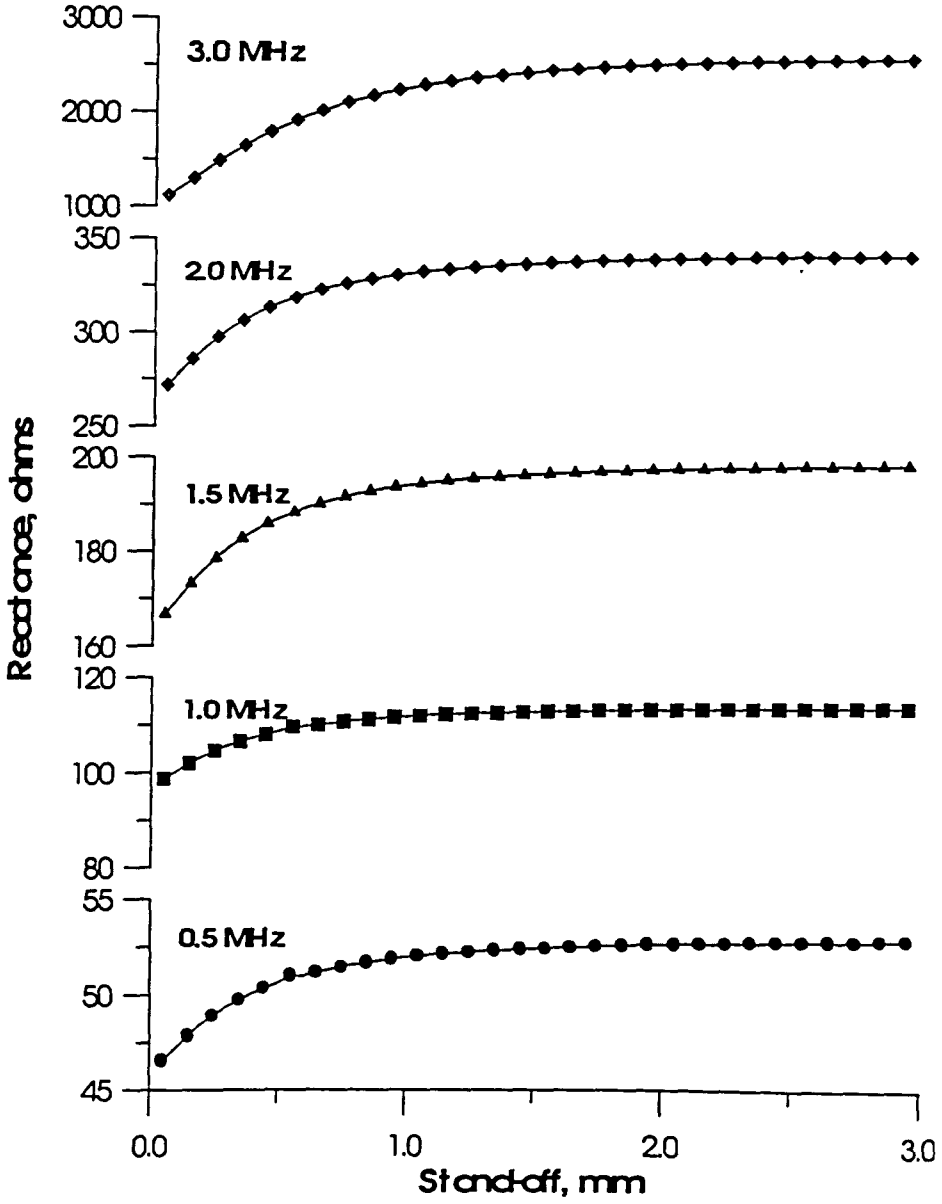

Figure 3.2: Effect of operating frequency on lift-off signal for the 500-kHz absolute probe

3.3.2 Probe Construction

The imaginary component of the impedance was measured at different lift-off distances for all three probes at the same frequency. The highest frequency (3 MHz), which gave the best results was selected. Figure 3.3 shows the lift-off signals of the three probes plotted on the same graph on a logarithmic scale. A large displacement between the three curves can be observed. The interpretation of this phenomenon is the following: at 3 MHz, the 500 kHz probe has the strongest signal (see figure 3.1), because it has the lowest resonant frequency. The 1 and 2 MHz probes have higher resonant frequencies and therefore have weaker signals at 3 MHz, respectively.

In view of this, the 500 kHz probe was selected as the inductive sensor to be used for the remaining experiments.

3.3.3 Workpiece conductivity

As can be seen from equation (2.2) of Dodd and Deeds calculations, the probe impedance is a function of the conductivity of the specimen. The measurements performed on different samples were to be correlated with the theoretical prediction described by relation (2.2).

For this purpose three specimens made of different conductive materials were selected. They were: aluminum, titanium and steel. While the conductivity of aluminum has the largest value (around 3×10^7 S/m), the conductivity of titanium and steel are very similar to each other (between 0.5×10^6 and 1.5×10^6 S/m). Figure 3.4 shows the lift-off signals obtained by measuring the three specimens with the 500 kHz probe at 3 MHz. It can easily be observed that aluminum, which has the largest conductivity value, has the lowest reactance, and that the curves for titanium and

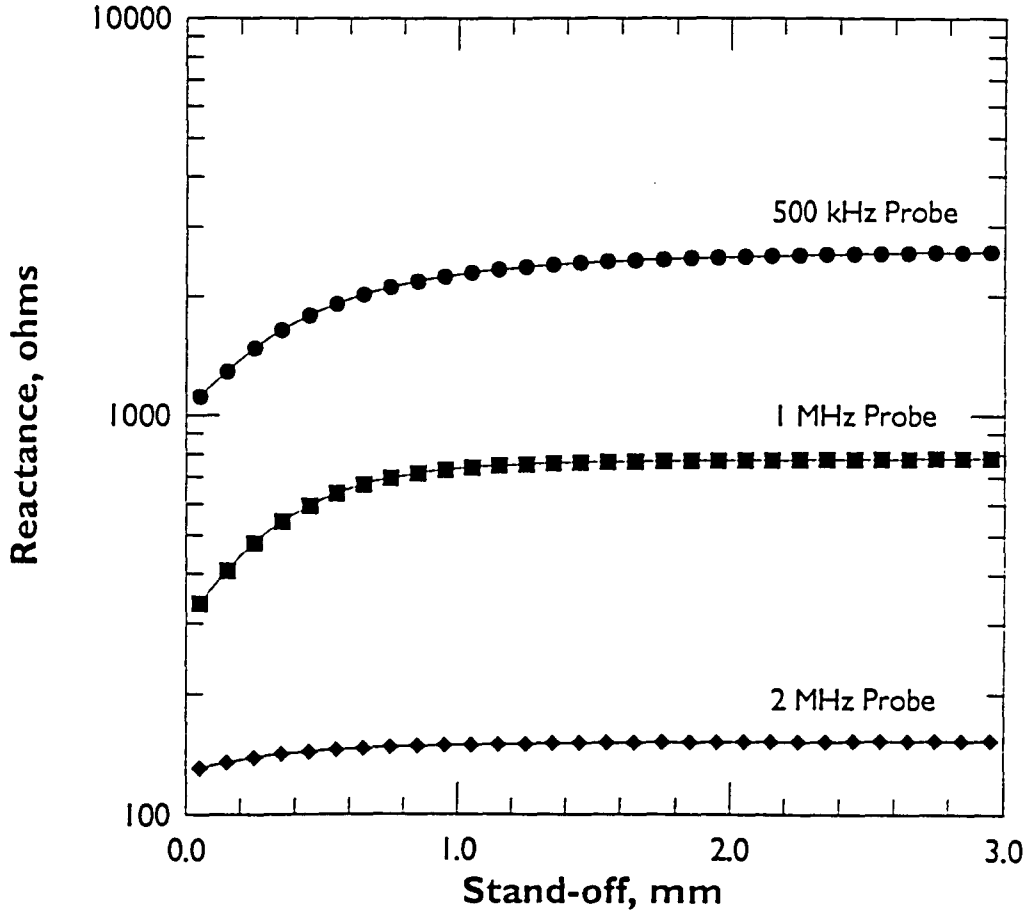

Figure 3.3: Lift-off signals for three probes at 3 MHz operating frequency

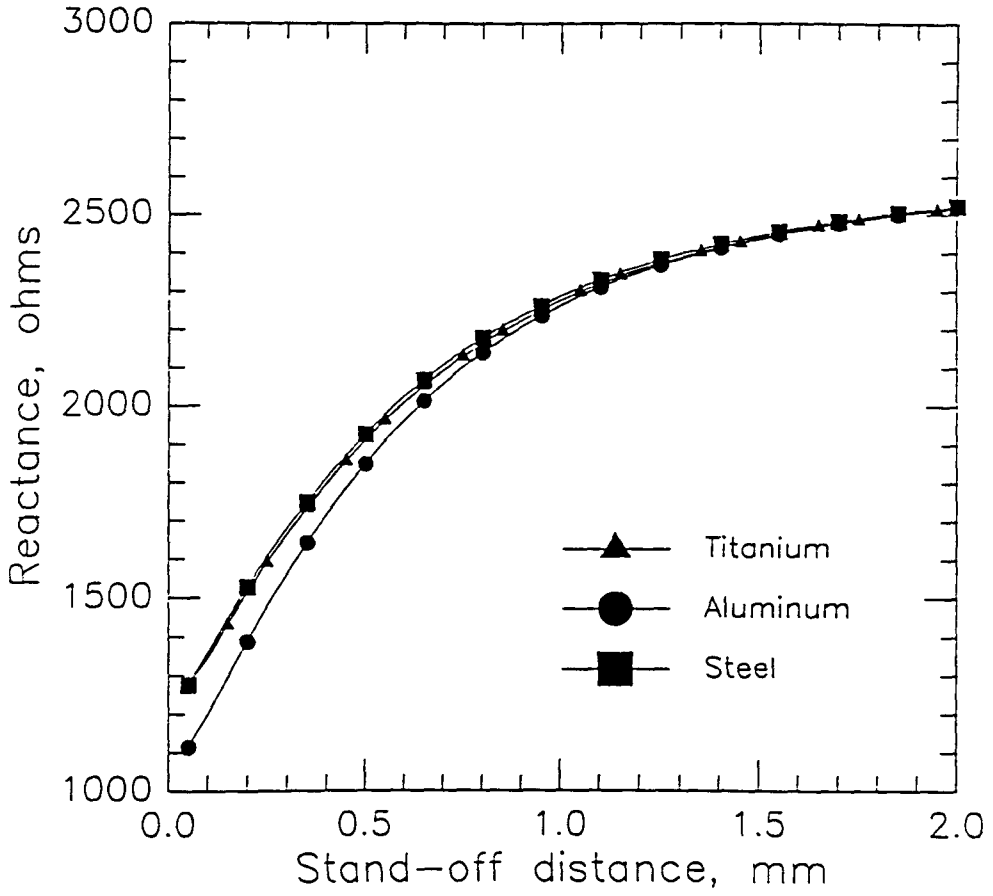

Figure 3.4: Effect of workpiece conductivity on lift-off signal [500-kHz probe at 3 MHz operating frequency]

steel almost overlap. This is in conformity with relation (2.2).

A general conclusion can be made by analyzing Figures 3.2, 3.3 and 3.4 in reference to the shape of the curves. If the lift-off distance is increased beyond 2 or 2.5 mm, the curves tend to saturate. This gives a good measure for the range of distances at which inductive sensors are useful. This performance measure will be analyzed in greater detail in the next few chapters.

CHAPTER 4. INFERRING SURFACE TOPOGRAPHY USING INDUCTIVE SENSORS

4.1 Overview

Inductive sensors may be used to produce images of geometrical discontinuities in a specimen being inspected. If the diameter of the eddy current probe is small compared to the size of the discontinuity, an accurate two-dimensional image that shows the extent and shape of the discontinuity can be obtained.

Based on the relationship between inductive reactance of the probe and changes in lift-off, a method for obtaining the "real image" of the specimen surface will be presented in this chapter. While robot vision sensors furnish detailed information about the shape and orientation of the object at a relatively long distance, inductive sensors are best suited to provide information relating to proximity and position at short distances. Based on the results of several tests, both qualitative and quantitative measures for determining lift-off will be given in the following chapters.

4.2 Fabrication of a Test Specimen with Variety of Surface Features

At the Center of NDE, an automated system for acquiring the imaginary and real part of the impedance of a probe as it scans a specimen under computer control has been built. The probe (or the specimen) can be stepped along in raster fashion

in programmable increments. An HP-4194A impedance analyzer is used to measure the impedance of the coil. The impedance values are digitized and stored on the hard drive of the PC for off-line processing. Everything is controlled from the PC through menu-driven software. A detailed description of the software structure and hardware configuration is given in Chapter 6.

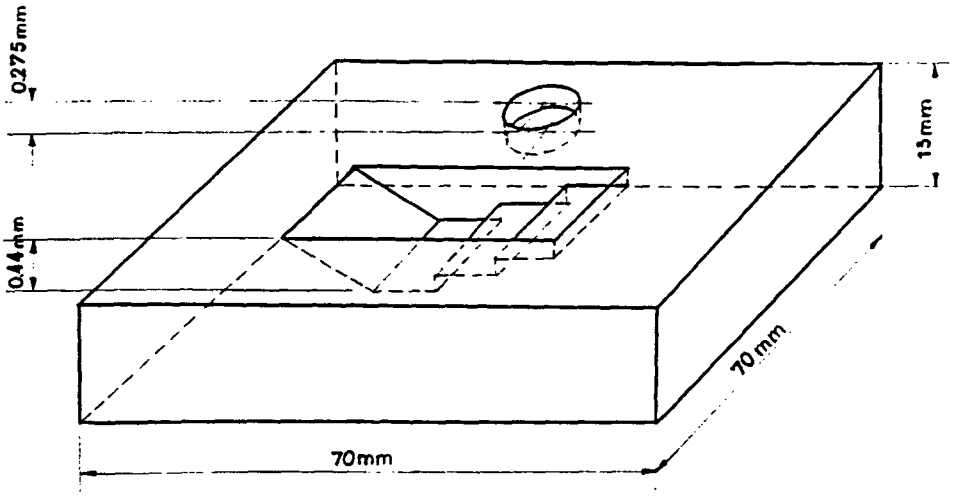

Figure 4.1: Test sample containing various surface features

A test block containing various surface features was designed and used as a specimen. The test sample, made from a rectangular plate of Al 6061 of dimensions $70 \times 70 \times 13\ mm^3$, is shown in Figure 4.1. The aluminum specimen was machined to have a number of surface features including three rectangular steps, a gradual incline,

and a circular indentation of fixed depth (275 micrometers). The lowest point of the surface, considering the flat plate level as reference, is at 440 micrometers below reference.

After the sample was fabricated, two different scans were performed: the first included the circular hole, the second, a region containing three steps and a gradual incline. Both 2-D scans were taken with the probe at a fixed height of about 200 micrometers above the reference level at a fixed frequency, 3 MHz. For scanning, the probe previously determined to be the best for monitoring lift-off, the 500 kHz probe, was used. An impedance map of the corresponding surface region was obtained for each scan. The data points in the map determine the probe impedance as a function of the coil-center position (x,y).

4.3 Probe Calibration Curve Modeled by a Polynomial Fit

Calibration of eddy current measurement systems [34] is an important prerequisite for attaining the degree of accuracy that quantitative nondestructive evaluation measurements require. In the case of inductive sensors, the relationship between absolute imaginary impedance and changes in lift-off, can be modeled using a polynomial fit. This is required for processing the impedance map into a surface topography map that gives a "real image" of the specimen surface. The polynomial fit will be used later to actively control and adjust the lift-off during automated scans of objects with complex geometry.

To achieve the above mentioned goal, a program which collects data and generates the calibration table for lift-off increments of 0.01 mm was developed. Different polynomial fits and other classes of functions were evaluated in order to mathemat-

ically model the discrete calibration dependence. For searching the appropriate fit, the *Grapher*^{TM} software package available for DOS systems was used. This software allows one to choose from six classes of function and in the case of polynomial fits to choose the order of the polynomial. The best results were obtained using a 6th degree polynomial. For the polynomial fit, Grapher computes both the standard coefficients and the orthogonal and recursion factors. Two routines to calculate the polynomial fit were developed: one calculates values of a polynomial using the coefficients of the powers of x, and the other calculates the values using the orthogonal and recursion factors. For the latter routine, Clenshaw's recurrence formula, which is an efficient way to evaluate a polynomial [35] was used. This formula uses α_k and β_k as the recursion factors and c_k as the orthogonal factors of the polynomial in the following recurrence relation:

$$q_{N+2} = q_{N+1} = 0$$

$$q_k(x) = (x - \alpha_{k+1})q_{k+1}(x) - \beta_{k+1}q_{k+2}(x) + c_k \tag{4.1}$$

where k = N,N-1,...,1 and N is the degree of the fit.
It was shown [36] that this recurrence is such that the value of the polynomial at a point x is equal to $q_0(x)$.

Comparing results calculated using each of the two routines with the measured data points, it was observed that results using standard polynomial coefficients were quite inaccurate compared to the ones obtained using orthogonal expansions. This observation agrees with the mathematical justification provided by Ralston and Rabinowitz [36]. In Section 6.3 of their book, they explain that standard polynomials fail due to the ill-conditioned matrix obtained in the least-squares approximation, and justify the use of orthogonal polynomials to obtain more accurate results.

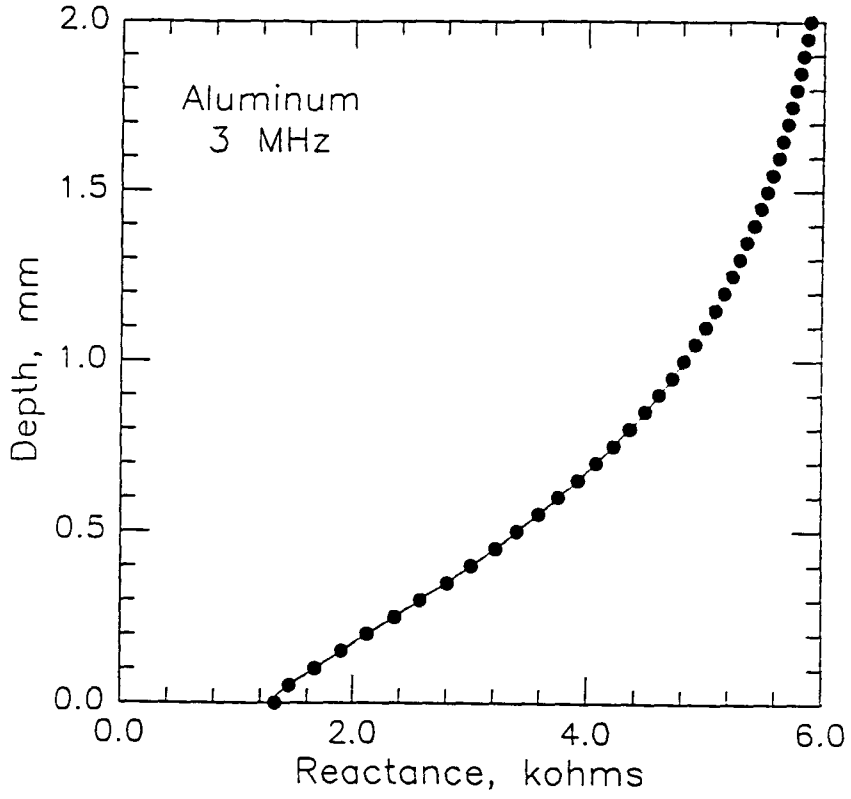

Figure 4.2: Calibration curve modeled by an orthogonal polynomial fit

As a result of this investigation, the critical routine which transforms impedance values to generate corresponding lift-off values with a good accuracy was developed. The polynomial approximation function for the 500 kHz probe and for 3 MHz operating frequency is illustrated in Figure 4.2. For a particular measurement system, the calculation of the calibration function depends upon the inductive sensor used, the operating frequency, and the conductivity of the specimen. An important note must be made with regard to selecting the appropriate operating frequency. The frequency has to be close to the resonant frequency of the coil, but less than the lowest resonant

frequency obtained at the highest possible value of lift-off distance. This is necessary to maintain a monotonic response of the sensor to changes in height.

4.4 Inferring Specimen Surface Topography from Impedance Maps

Using the calibration curve routine, we can now transform an impedance map into a height (depth) profile map. The map describes the actual surface topography of the specimen. The transformation is accomplished by a program which utilizes the calibration routine for each data point. This off-line implementation was incorporated later in the menu-driven scanning software.

Figure 4.3 shows first, the impedance map of the circular hole. The "depth" map is subsequently inferred from the impedance map. Figure 4.4 shows the results of applying the transformation in the region that includes the three steps and the gradual incline. An important observation to be made is that the dimensions of surface features in the depth map correspond very closely with the ones measured on the real sample. This is a significant result that demonstrates the accuracy of eddy current sensors. *We can conclude that the sensitivity of the inductive sensor used is such that variations as small as a few micrometers can be determined accurately.* This important fact will later determine whether inductive sensors can be used to actively follow a surface with success. It is clear, however, that the accuracy of this method depends on the accuracy of the calibration curve.

One of the complicating factors discovered during the experiments was that the relatively large diameter of the probe (1.5 mm) blurs the edges of the milled region. This causes difficulties in determining the precise location of corners and steps. In general, the size of an inductive sensor is limited by fabrication technology. If the

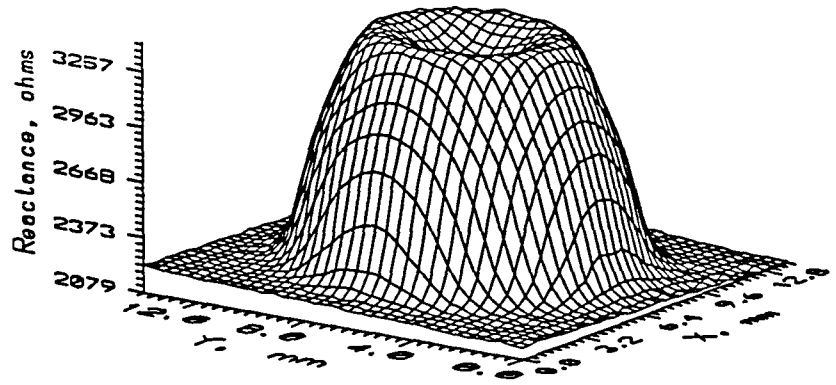

Impedance Map

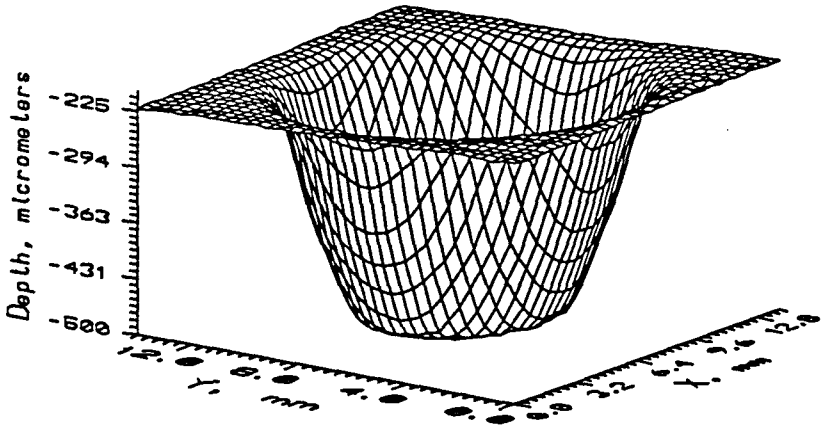

Depth Map

Figure 4.3: Mapping surface features: flat-bottomed hole

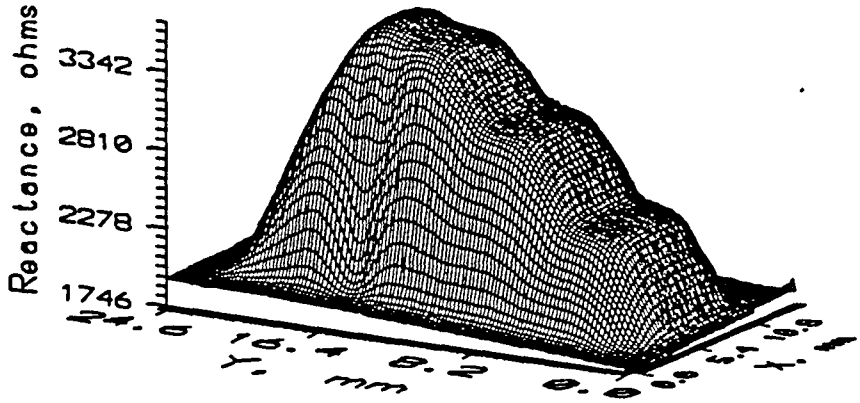

Impedance Map

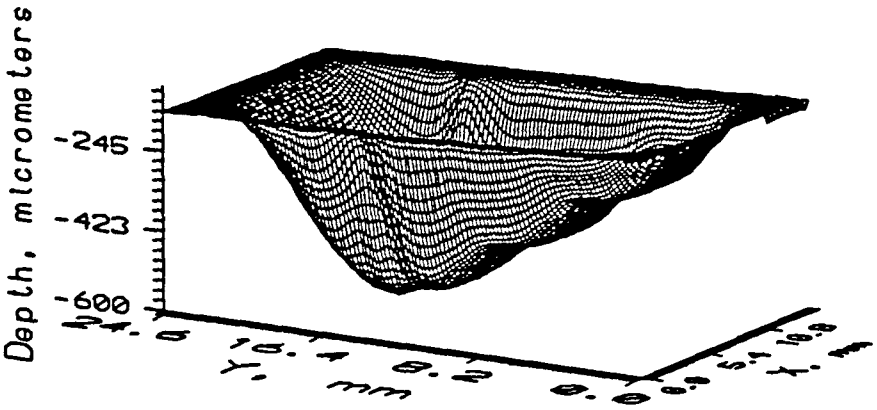

Depth Map

Figure 4.4: Mapping surface features: linear slope and three steps

dimensions of a discontinuity on the surface is smaller than the size of the sensor, the resolution of the height map in that region is significantly diminished. In order to improve the resolution of the sensor, the use of image processing techniques was investigated. The next chapter describes the results of this investigation.

CHAPTER 5. METHODS FOR IMPROVING THE RESOLUTION OF INDUCTIVE SENSORS

5.1 Overview

In the past nondestructive evaluation methods have been used primarily to provide qualitative information regarding the presence or absence of a flaw. However, the measured data also contain quantitative information about the size, shape, location and orientation of flaws, as well as other details such as the shape of the specimen surface. Imaging provides a means for presenting this information in a convenient way for human interpretation.

An eddy current image can be obtained by processing the data acquired by scanning the specimen using an eddy current probe in a raster pattern at a fixed distance above the test piece. The purpose of the image processing is to improve the resolution of the measurement system.

Two basic image enhancement techniques can be employed for improving resolution: spatial domain methods and frequency domain methods. The spatial domain refers to the image plane itself, and methods in this category are based on direct manipulation of pixels in an image. Frequency domain processing techniques are based on modifying the Fourier transform of an image.

Frequency domain methods rely on the convolution theorem. The output pro-

duced by an inductive probe scanning over an arbitrary discontinuity can be represented as the convolution of the true image with the response of the probe to a point imperfection [37]. This latter response is called the point spread function of the probe. Hence, in order to obtain the true image the procedure to follow is to deconvolve the measured probe response with its point spread function. The difficulty associated with using this method is that a general method for computing the point-spread function for different probe systems for evaluating their imaging characteristics does not exist.

The approach taken in this chapter is that of the spatial domain method. The goal is to obtain contrast enhancement and edge detection.

5.2 Spatial Domain Image Processing Techniques Adequate for Edge Detection and Enhancement of Eddy Current Images

Edge detection and image enhancement techniques are very much problem-oriented. Thus, for example, a method that is suitable for enhancing x-ray images may not necessarily be the best approach for enhancing an eddy current image. This section describes a few techniques that have shown some merit for processing eddy current images.

An edge is the boundary between two regions with relatively distinct gray-level properties [38]. We make the assumption that the regions are sufficiently homogeneous so that the transition between two regions can be determined on the basis of gray-level discontinuities alone.

The basic idea in most edge-detection techniques is the computation of a local derivative. Figure 5.1 illustrates the principle of this idea. It shows an image of a

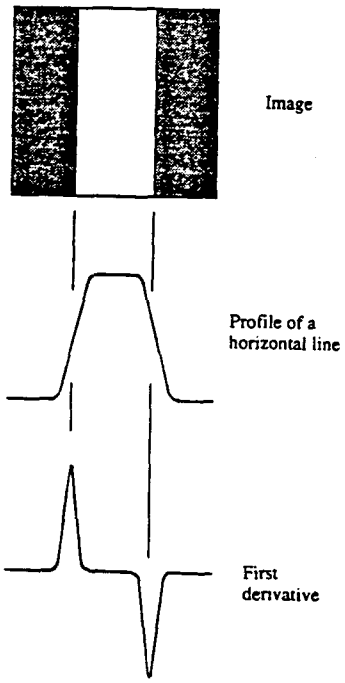

Figure 5.1: Edge detection using derivative operators [38]

light stripe on a dark background, the gray-level profile along a horizontal scan line of the image, and the first derivative of the profile. It can be observed from the profile that an edge (transition from dark to light) is modeled as a smooth, rather than as an abrupt, change of gray level.

Figure 5.1 shows that the first derivative of the gray-level profile is positive at the leading edge of a transition, negative at the trailing edge, and zero in areas of constant gray level. The magnitude of the first derivative can be used to detect the

presence of an edge and the sign to determine the transition orientation.

The Laplacian (the second derivative), which is a good high-pass filter, can also be used for the purpose. However, it is not a particularly good tool for demarcating edges. The Laplacian gives a larger response to a line than to a step, and to a point than to a line. In an image that contains noise, typically present as points varying in brightness (which is frequently the case in eddy current images), the Laplacian will show such points more strongly than the edges or boundaries that are of interest.

So far the discussion has been limited to a one-dimensional horizontal profile. A similar argument applies to an edge of any orientation in the image. Therefore, the best approach to locating edges is to use first derivatives in two (horizontal and vertical) or more directions.

The most common method of differentiation in image processing applications is the gradient. For an image f(x,y), the gradient of f at coordinates (x,y) is defined as the vector

$$\nabla \mathbf{f} = \begin{bmatrix} \frac{\partial f}{\partial x} \\ \frac{\partial f}{\partial y} \end{bmatrix} = \begin{bmatrix} G_x \\ G_y \end{bmatrix} \tag{5.1}$$

From vector analysis it is known that the gradient vector points in the direction of maximum rate of change of f at (x,y). In edge detection an important quantity is the magnitude of this vector, generally referred to simply as the gradient and denoted ∇f, where:

$$\nabla f = mag(\nabla \mathbf{f}) = [\mathrm{G_x^2} + \mathrm{G_y^2}]^{1/2} \tag{5.2}$$

This quantity gives a measure of the maximum rate of increase of f(x,y) per unit distance in the direction of ∇f. The usual procedure is to approximate the gradient with absolute values

$$\nabla f \approx | G_x | + | G_y | \tag{5.3}$$

rather than using (5.2). This calculation is easier to perform and is preferred especially when implemented in digital hardware.

w_1	w_2	w_3
w_4	w_5	w_6
w_7	w_8	w_9

Figure 5.2: A general 3×3 mask

The usual way to look for discontinuities is to run a mask through the image. For the 3×3 mask shown in Figure 5.2, the procedure involves computing the sum of products of the coefficients with the gray levels contained in the region encompassed by the mask. That is, the response of the mask at any point in the image is

$$R = w_1 z_1 + w_2 z_2 + ... + w_9 z_9 \tag{5.4}$$

where z_i (i=1,2,...,9) is the gray level of the pixel associated with mask coefficient w_i. The response of the mask is defined with respect to its center location. When

the mask is centered on a boundary pixel, the response is computed by using an appropriate partial neighborhood.

Equations (5.1) and (5.2) show that computation of the gradient of an image is based on obtaining the partial derivatives $\frac{\partial f}{\partial x}$ and $\frac{\partial f}{\partial y}$ at every pixel location. There are several ways to implement derivatives in digital form. Table 5.1 lists some gradient operators that have been used with success on eddy current images. Computation of the gradient at the location of the center of the masks utilizes equation (5.2) or (5.3), which gives one value of the gradient. To get the next value, the masks are moved to the next pixel location and the procedure is repeated. Thus, after the procedure has been completed for all possible locations, the result is a gradient image of the same size as the original image.

The Prewitt, Sobel, and Isotropic operators from Table 5.1 compute horizontal and vertical differences of local sums. This reduces the effect of noise in the data [39]. It can be observed that these operators have the desirable property of yielding zeros for uniform regions. Considering Sobel as an example [38], derivatives based on the Sobel operator masks are

$$G_x = (z_7 + 2z_8 + z_9) - (z_1 + 2z_2 + z_3) \tag{5.5}$$

and

$$G_y = (z_3 + 2z_6 + z_9) - (z_1 + 2z_4 + z_7) \tag{5.6}$$

where, as before, the z's are the gray levels of the pixels overlapped by the masks at any location in an image.

Another useful image processing technique, that has significant effects on eddy current images is histogram equalization. A cumulative distribution of pixel intensi-

Table 5.1: Three types of gradient operators [Note that all mask coefficients sum to 0, indicating a response of 0 in constant areas]

	horizontal	vertical
Prewitt	$\begin{bmatrix} -1 & -1 & -1 \\ 0 & 0 & 0 \\ 1 & 1 & 1 \end{bmatrix}$	$\begin{bmatrix} -1 & 0 & 1 \\ -1 & 0 & 1 \\ -1 & 0 & 1 \end{bmatrix}$
Sobel	$\begin{bmatrix} -1 & -2 & -1 \\ 0 & 0 & 0 \\ 1 & 2 & 1 \end{bmatrix}$	$\begin{bmatrix} -1 & 0 & 1 \\ -2 & 0 & 2 \\ -1 & 0 & 1 \end{bmatrix}$
Isotropic	$\begin{bmatrix} -1 & -1.414 & -1 \\ 0 & 0 & 0 \\ 1 & 1.414 & 1 \end{bmatrix}$	$\begin{bmatrix} -1 & 0 & 1 \\ -1.414 & 0 & 1.414 \\ -1 & 0 & 1 \end{bmatrix}$

ties is calculated and used as an intensity transfer function. The procedure attempts to equalize the number of pixels at each intensity. This can help increase contrast in images that have a majority of pixel intensities spanning a small range of values. In terms of enhancement, this result implies an increase in the dynamic range of the pixels, which can have a considerable effect on the appearance of an image.

5.3 Improving Sensor Resolution and Locating Sharp Changes in Height

The menu-driven software, which controls the whole process of scanning an inductive sensor above a specimen, stores the impedance data in Surfer format files. These files can be visualized on a PC by using the $Surfer^{TM}$ software package. The two milled regions of the manufactured test piece could be seen in Figure 4.3 and 4.4, as Surfer plots.

The 2-D surface topography maps of the two regions were transferred to the DEC workstation and sectored into 8-bit gray scale format. HAPPI, an image processing software package developed in the ISU Electrical and Computer Engineering Department and CNDE, was then used. A wide variety of image processing routines has been incorporated into HAPPI. These routines range from commonly known and implemented algorithms to routines that were developed specifically for x-ray radiograph NDE image processing tasks. For eddy current purpose, two categories of routines were mainly used: contrast enhancement and edge detection.

First, image enhancement results obtained for the region with the circular hole will be presented. Figure 5.3 shows the original image and a vertical cross section plot. The cross section plot illustrates pixel intensity as a function of position along the central vertical cross section. After applying several image processing routines (histogram equalization and Isotropic edge detection were among them), the image shown in Figure 5.4 was obtained. Of significant interest is the vertical cross section plot which shows a dramatic improvement in locating the corners of the circular hole. Measurements performed on the image were compared with measurements performed on the real sample. The distance between the two peaks on the plot corresponded

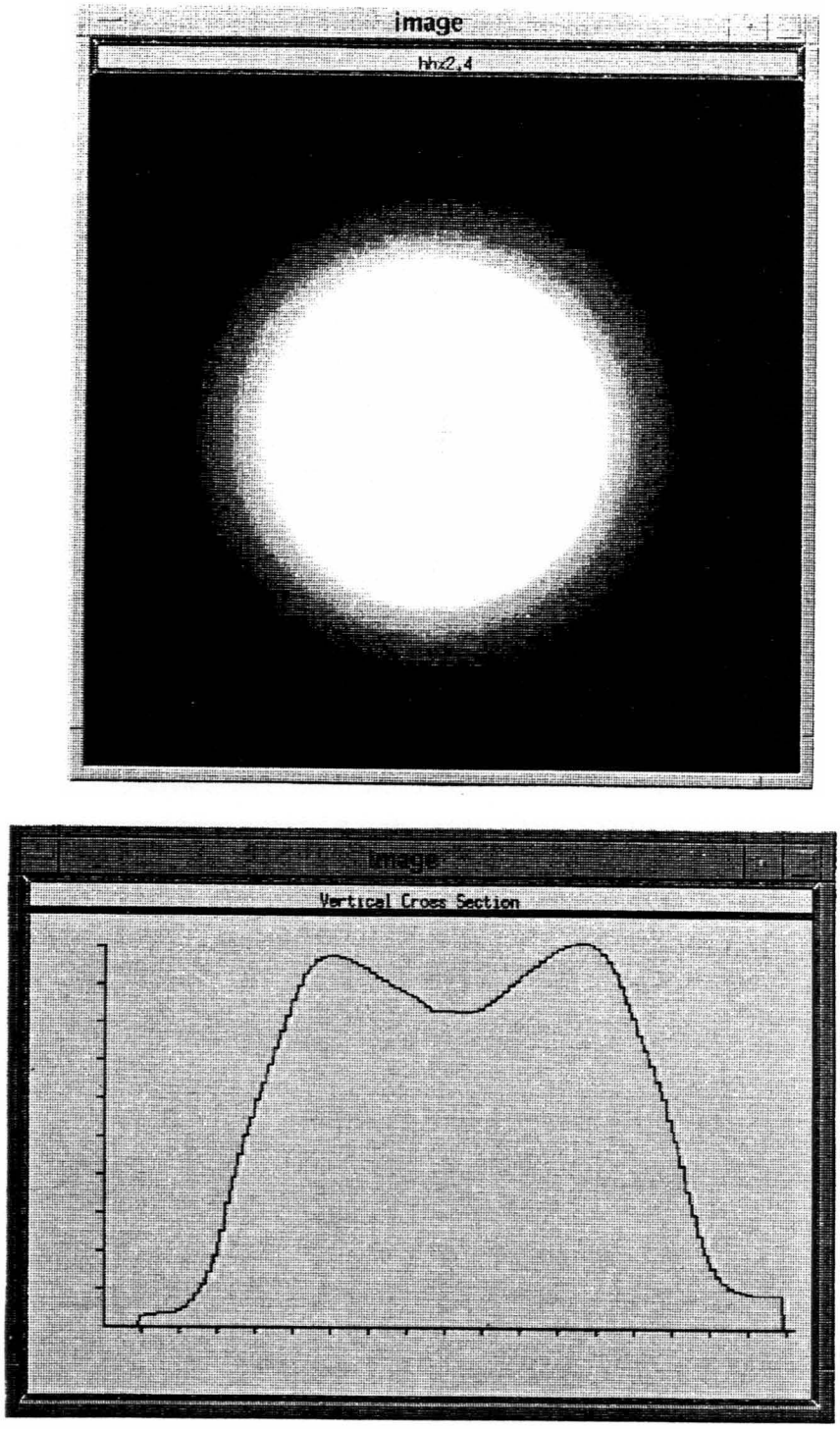

Figure 5.3: Initial image of the circular hole region

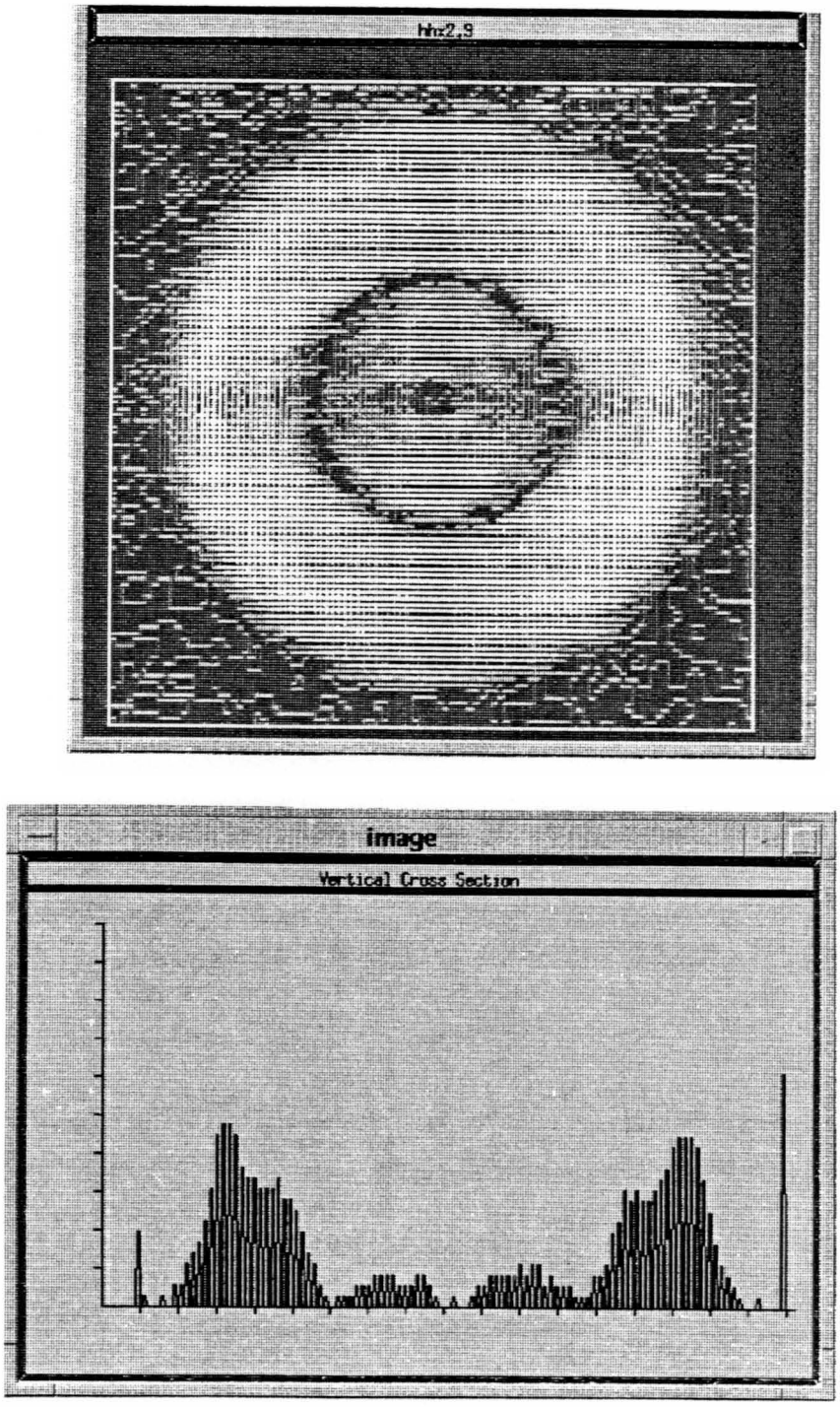

Figure 5.4: Processed image of the circular hole region (histogram equalization, Isotropic edge detection)

proportionally with the diameter of the hole. The error was below 5%. This shows that for this type of simple geometry, location of edges can be performed with good precision.

The original image and the corresponding vertical cross section of the second region (with three steps and gradual incline) are presented in the upper part of Figure 5.5. At the bottom of the same figure, the processed image (histogram equalization and Isotropic edge detection) can be seen. We can compare the processed image with the original image, and also with the original image in topographic format produced by Surfer on a PC (see Figure 5.6). Figure 5.7 shows two other processed images (based on the same original image) obtained by using Sobel and Prewitt edge detectors. Image processing for the second region led to significant improvements also.

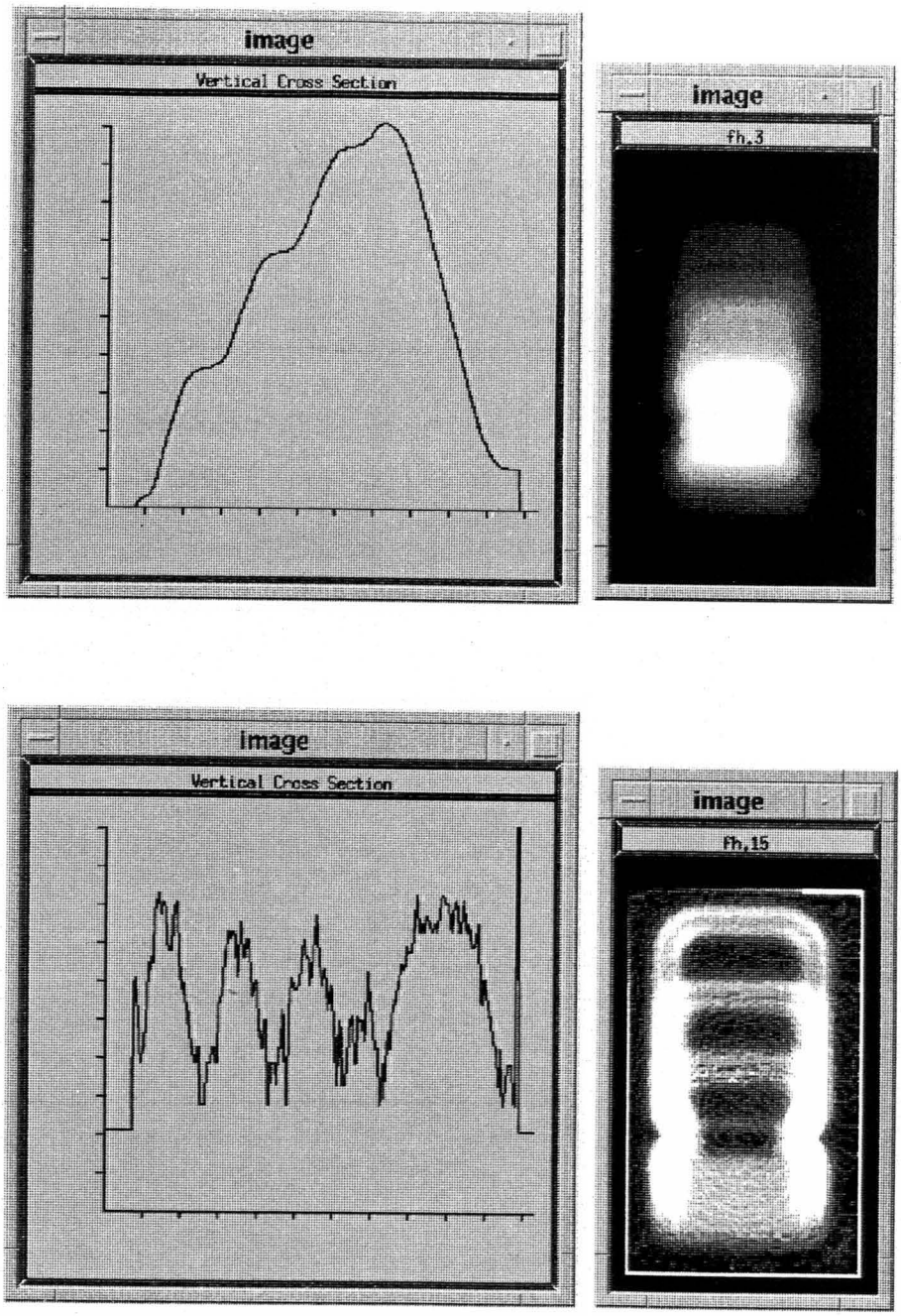

Figure 5.5: Initial image and processed image (histogram equalization, Isotropic edge detection) of the region with three steps and gradual incline

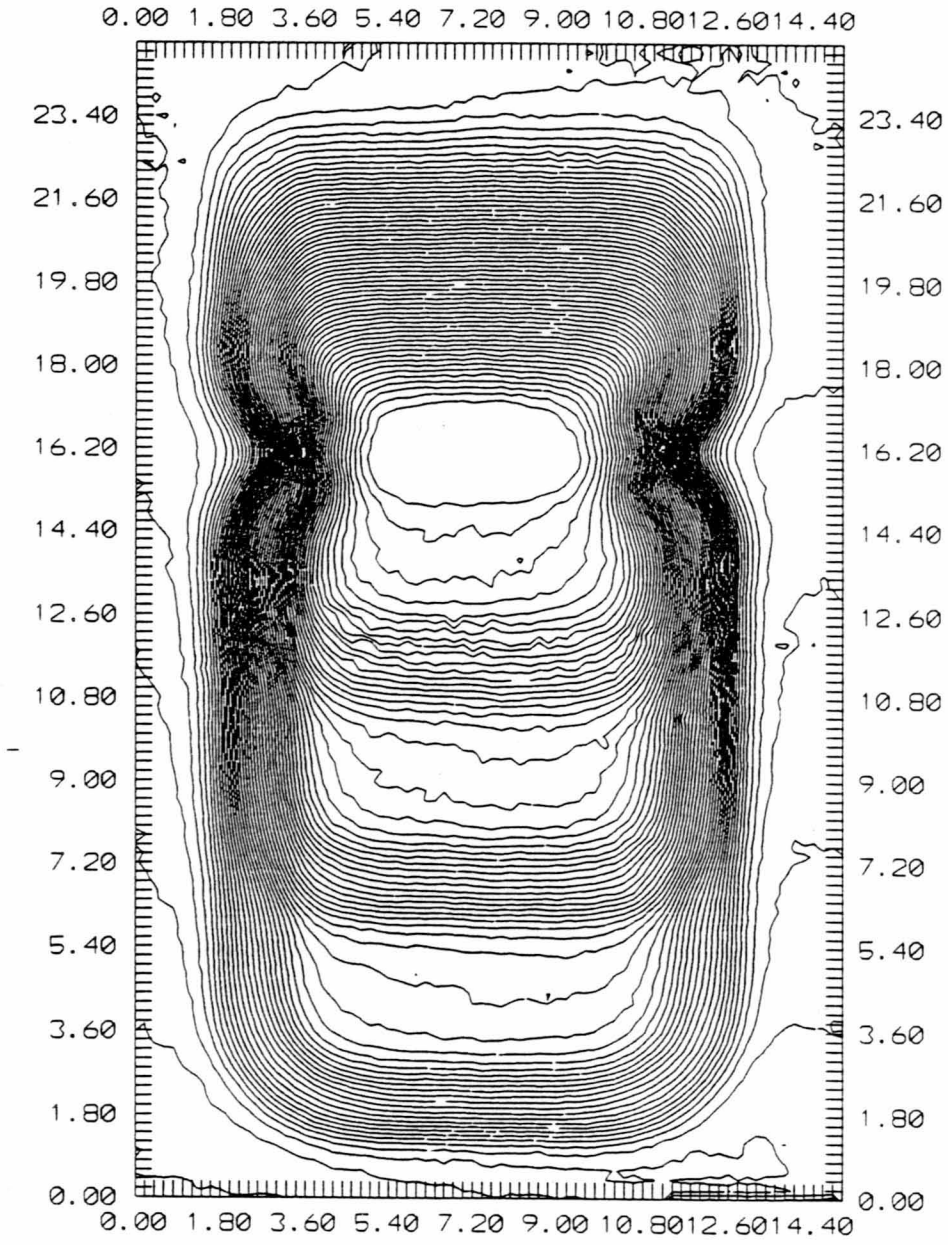

Figure 5.6: Initial image of the region with three steps and gradual incline (topographic view of the Surfer format file)

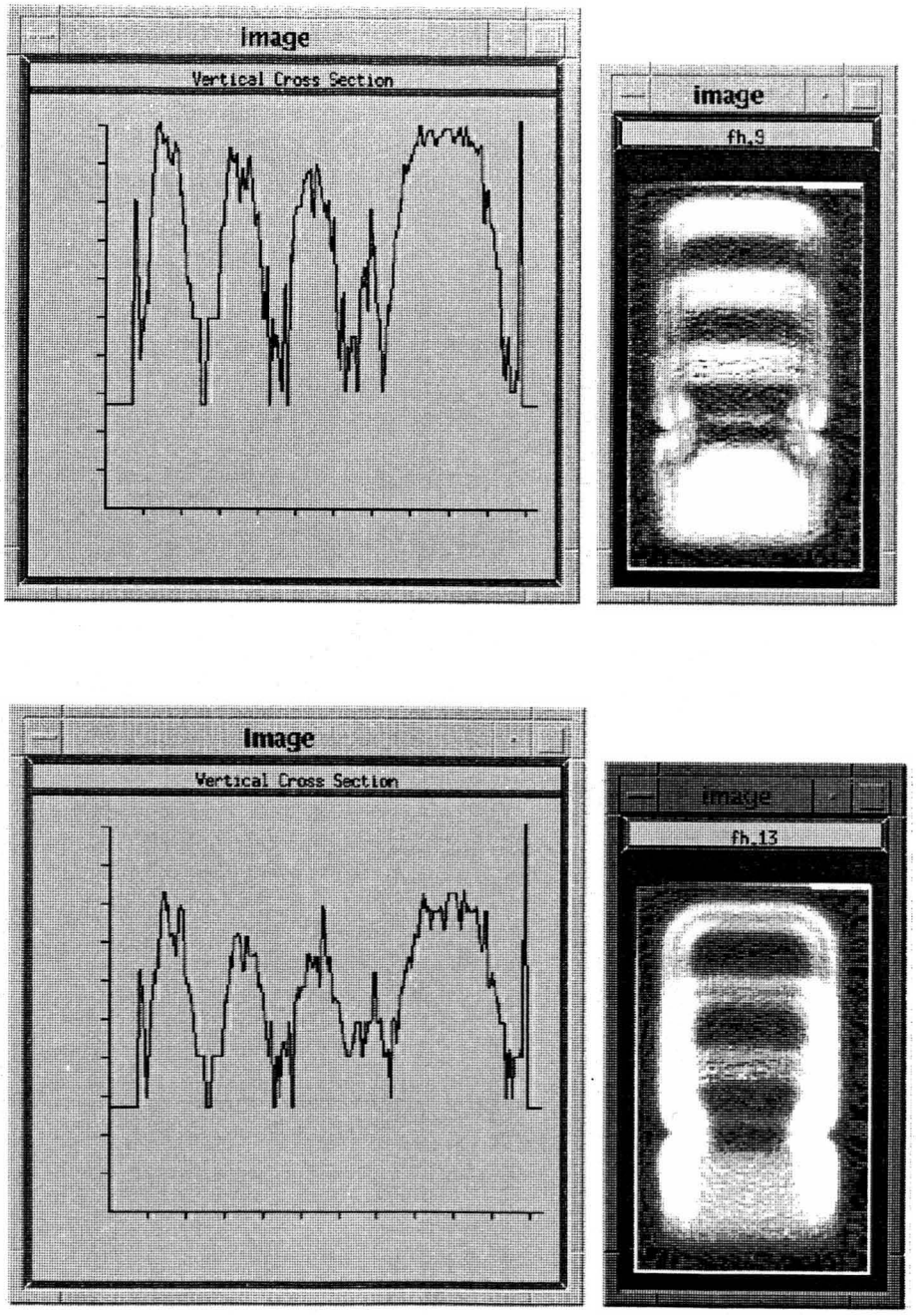

Figure 5.7: Processed images (top: Sobel edge detector; bottom: Prewitt edge detector) of the region with three steps and gradual incline

CHAPTER 6. SOFTWARE CONSIDERATIONS IN DEVELOPING THE MEASUREMENT SYSTEM

6.1 General Hardware Configuration

The eddy current measurement system developed at the Center for Nondestructive Evaluation in the test bed lab is composed of three major subsystems:

1. Scanning subsystem
2. Impedance analyzer and eddy current probe subsystem
3. Computer subsystem.

Figure 6.1 illustrates the role played by each subsystem in the configuration of the measurement system.

The scanning subsystem, which is presented schematically in Figure 6.1, includes two 4-degree-of-freedom motion control scanners and a programmable motion controller. The two scanners can execute x,y and z translations as well as rotations. For the task on hand, only x,y translations have been used for raster scans over an entire area of the specimen, and z translations for lift-off compensation.

The HP 4194A impedance analyzer is used to measure the eddy current probe impedance over a broad frequency range (100 Hz to 15 MHz). The impedance measuring procedure is based on the phasor voltage/current ratio method, whereby the probe impedance is obtained by determining the phasor ratio between the applied

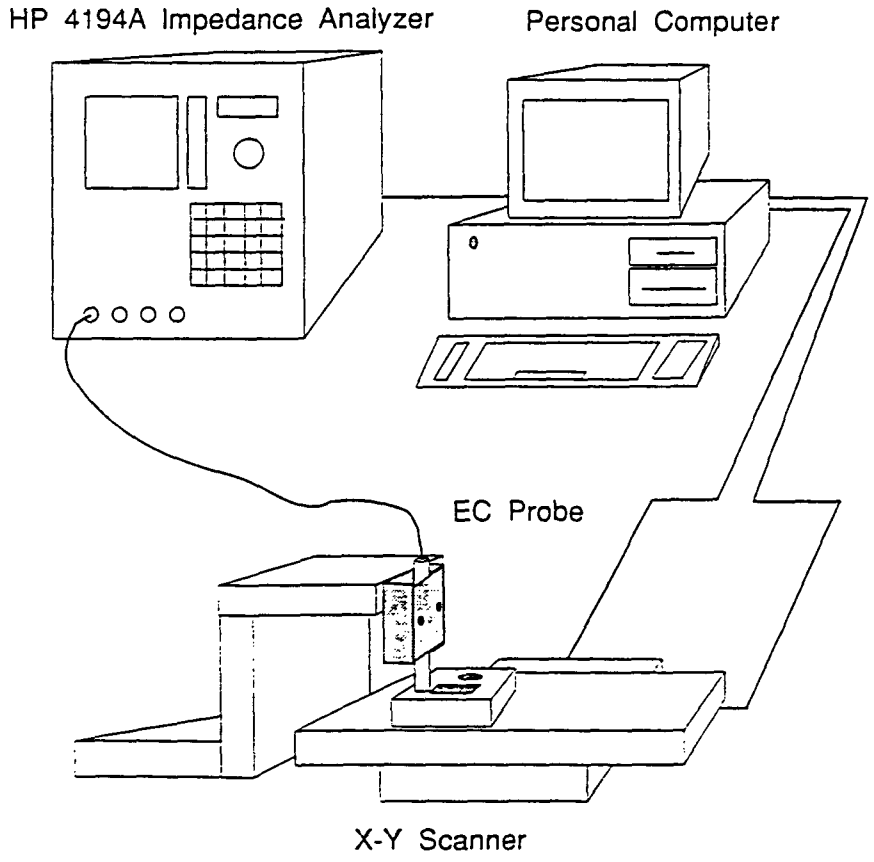

Figure 6.1: Test bed eddy current measurement system

test signal voltage and the current flowing through the probe. In order to cover a broad frequency range, the impedance analyzer performs measurements by using an autobalance bridge circuit.

The computer subsystem controls the operation of the entire system: collecting, storing, analyzing, and displaying the data. It houses a GPIB plug-in card, which interfaces the computer to the impedance analyzer and the motion controller through the IEEE-488 standard bus. The data are exchanged asynchronously between the

devices at a rate of almost 1 Mbytes/s. Each of the three GPIB devices (computer, impedance analyzer, and motion controller) is capable of performing one or more of the following interface functions:

1. Listener - A device capable of receiving data over the interface when addressed to listen.

2. Talker - A device capable of sending data over the interface when addressed to talk. There can be only one active talker at a time.

3. Controller - A device capable of specifying a talker and listener for a data transfer (including itself). This function is performed only by the computer.

Implementation and control of these functions were incorporated in high level GPIB routines, which allow convenient access to devices.

6.2 Software Development

The control software was initially written using *Microsoft*^{TM} C for the IBM-PC. For the second version, the software was translated to *Borland*^{TM} C++, which allows a more flexible implementation as well as takes advantage of powerful C++ features. In addition, the second version incorporates a scanning routine employing a previously computed scan plan, that is dedicated to pin geometry measurements. This approach is limited by the complicated procedure of determining an appropriate scan plan and having to solve registration problems for the particular geometry.

A third version that uses a "no-scan plan" approach has also been implemented. The user defines the measurement parameters before each scan. The ultimate goal of this approach is to combine flexible scanning capabilities with surface sensing information.

6.2.1 Program User Interface

The testbed program is structured into a series of menus which allow the user to define a variety of parameters involved in a scan. Cursor keys are used to select individual menu items, and these are invoked when they are highlighted. Figure 6.2 shows the main menu hierarchy which the user must use to set up a run. The main menu is displayed when the program starts up, and each option has its sub-menu.

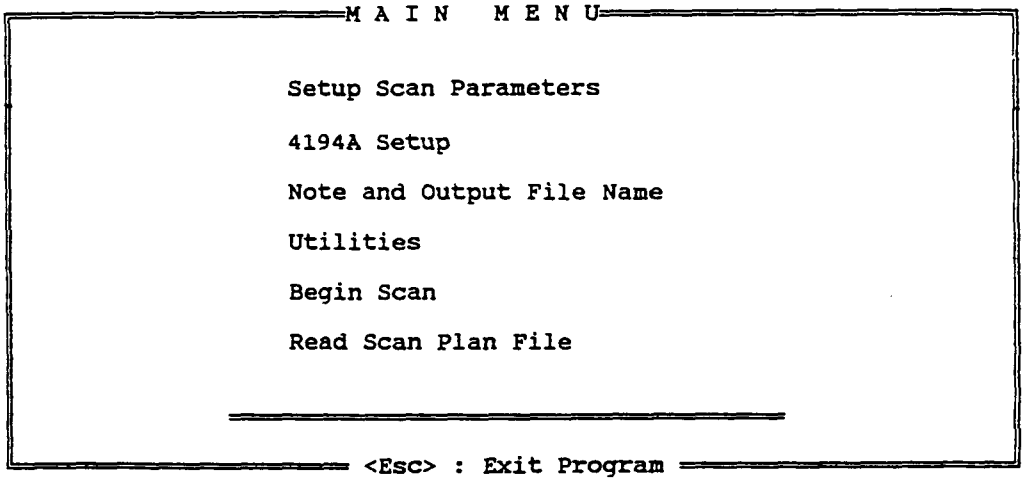

Figure 6.2: Main menu structure for testbed program

The user may choose from two procedures for scanning - either using a preexisting scan plan file described by the last menu item or by defining new scan parameters via the first menu item. The latter approach is illustrated in Figure 6.3, where motion along each axis may be programmed. The significant parameters are the length of

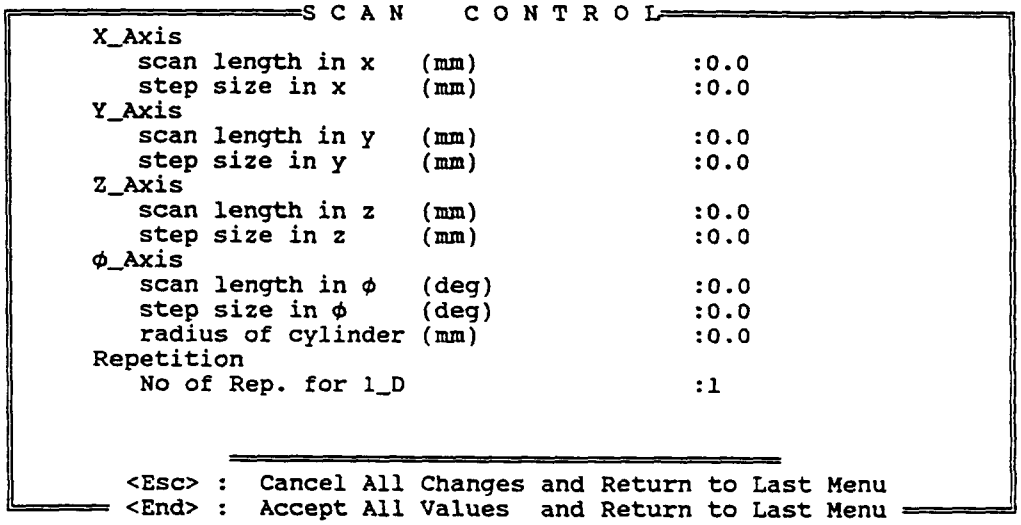

Figure 6.3: The scan parameters setup menu item

scan and the step size. For cylindrical geometries, the radius of the cylinder must be provided. If the user enters the parameters along only one axis then a line scan (1-D scan) is performed. If parameters along two axes are specified then an area scan (2-D scan) is executed. Area scans take longer, but produce complete field maps of probe impedance. At run time, the user-programmed values are incorporated into motion commands (referred to as X-command language in the manuals) and these are then sent to the motion controller for execution.

The impedance analyzer can be programmed using the "4194A Setup" menu item of the main menu. Figure 6.4 illustrates the parameters available for programming. Two parameters are of significant importance for setting the measurement speed: in-

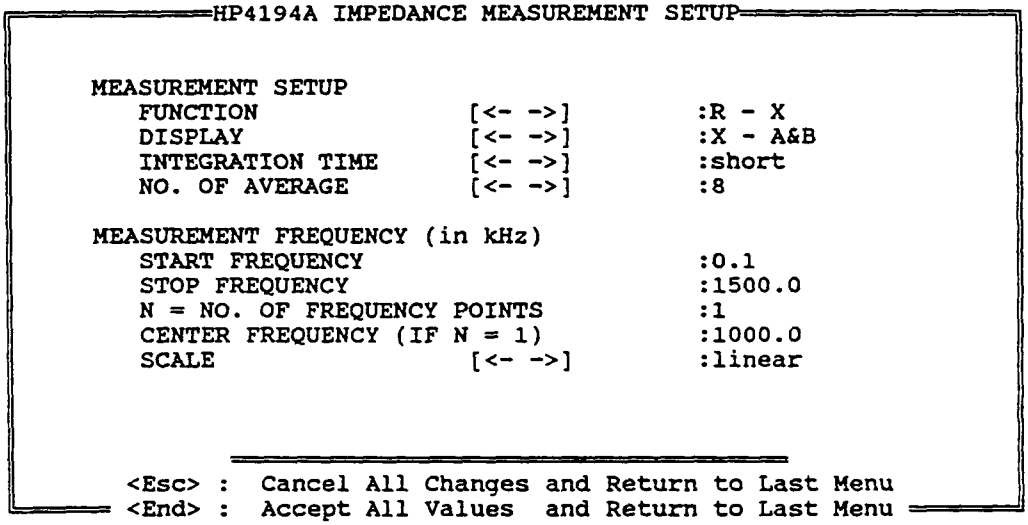

Figure 6.4: The impedance analyzer setup menu item

tegration time and number of measurements for averaging. The first parameter selects the digital integration time, where MED (5 msec) or LONG (100 msec) integration times minimize noise on the trace but increase the time spent for each measurement point. SHORT (0.5 msec), the default setting, has been the value mostly used in inductive sensor tests. The second parameter, the number of measurements for averaging, is useful for reducing the effects of noise on the final data image. The number can be set to 1, 2, 4, 8, 16, 32, 64, 128, or 256. The greater is the number of samples averaged, the greater will be the reduction in noise. It was observed that the fastest scan was obtained using SHORT integration time and "averaging factor" of 1, but this led to a high level of noise in the measurements. The trade-off between obtaining

smooth 2-D eddy current images and rapid scans must be determined by the user.

The testbed program can optionally save the user-defined parameters in a file, and also allow the user to create a text-based note file describing the scan. This is implemented in the "Note and Output File Name" menu item, which also allows the user to specify the output data file name. The "Utilities" option contains several commands for data processing, file manipulation, and manual axis movements. The "Begin Scan" option sets the scan in motion using the currently defined options. The scan can be interrupted at any time by the user by pressing the ESC key. This action not only stops the scan, but also returns the probe to the initial starting point.

6.2.2 Program Structure and Design Issues

The source code for the testbed program is organized in a large C language program implemented in the *Borland*^{TM} C++ environment. The software is structured in 18 modules as presented in Table 6.1, and was designed to be easy to maintain and add new features to at a later date. To achieve this goal, structured programming and object-oriented concepts were implemented. As the module description from Table 6.1 suggests, most of the module routines have been organized hierarchically at different control levels:

* low level GPIB interface
* high level device drivers and GPIB commands
* high level device control for dynamic binding of virtual devices
* high level scan and input control.

This programming technique improves software flexibility and makes the program much easier to work with.

Table 6.1: Source code modules used in the testbed program

Module	Description
TEST.C	Main program displaying the main menu
GPIBDRV.C	High level GPIB calls
DVCNTRL.C	High level device control routines
SCNCNTRL.C	High level motor control routines
MOTOR.C	Motor driver routines
DEVICE.C	Impedance analyzer driver routines
PIN.C	Pin geometry scan control
SCNPLN.C	User programmed scan control
READ_PLN.C	Scan plan data acquisition
SCREEN.C	Screen display functions
MENU.C	Menu item display and maintenance routines
MAIN_MEN.C	Menu item structures
REQUEST.C	User input control for device page setup
MTR_PAGE.C	Scan parameter setup page
IA_PAGE.C	Impedance analyzer setup page
UTL_PAGE.C	Utility menu setup page
PIN_PAGE.C	Scan plan file setup page
P_ERROR.C	Error message display

One of the complicating factors encountered during software design was the large number of global variables and declarations scattered throughout the 18 modules. This made it almost impossible to maintain or add new features to the program. A reduction in the number of global variables was accomplished by using structured programming techniques: grouping variables together in structures, extensive use of function parameters and header files. Grouping the variables into structures organizes the variables, making them easier to keep track of and makes operations on the group

possible. For example, the program contains several structures which group together configuration variables that relate to the same device or menu item. Other structures, like those that bind virtual devices, contain pointers to general-purpose functions and safety flags. The structured organization of the program provides an easy way to add new devices to the measurement system.

All these improvements to the control software have made the program much easier to work with from a programmer's perspective, and also more powerful, allowing the user to perform eddy current inspections faster and more accurately.

CHAPTER 7. RESULTS AND SUGGESTIONS FOR FUTURE WORK

7.1 Overview

This chapter describes some applications of inductive sensors which may have practical use in eddy current inspection. In the beginning, the inductive sensor method presented in this thesis will be applied to a "real-world" specimen, a turbine engine component, and then an algorithm for guiding the inductive sensor to follow a complex geometry surface will be introduced. Following the discussion a few concluding remarks will be presented. The last part of the chapter will present suggestions for future work. The approaches described here are part of a larger effort in the Center for NDE aimed at developing new methods for generating efficient scan plans and scanning strategies.

7.2 Application of the Inductive Sensor Method to Practical Problems

Qualitative and quantitative information about lift-off and characteristics of surface features was obtained in Chapters 4 and 5 for a manufactured test sample. The discontinuities investigated were regular geometrical features and the range of lift-off was between 0 and 0.7 mm. In what follows, the inductive sensor method will be applied to a more complex specimen, which will involve the use of a wider range of

lift-off distances.

Figure 7.1 shows a cross section of the turbine disk of a jet engine. On this structure the scanned region includes a small sector of the web of the disk, illustrated in Figure 7.2. The area was scanned at a fixed height with the probe touching the highest point of the region. Once again, the calibration function had to be calculated and applied to interpret the impedance data as variations in lift-off. Figure 7.3 shows first, the image of the impedance map obtained as a result of the scan, and then, at the bottom, the corresponding image of the surface height map is given. The surface height image shows similar geometrical features with the real shape of the scanned area on the turbine disk. As a quantitative measure of sensor capabilities, the same image shows that features as deep as 2.5-3 mm can be visualized and measured with good accuracy. Beyond this depth the image gets obscured by noise, due to the fact that saturation of the calibration curve becomes too severe.

We can therefore infer that inductive sensors can be used with good accuracy for a range of lift-off distances up to 2.5 mm, and the sensitivity of the probe is such that variations as small as a few micrometers can be determined with good precision. The main limitation of this method is that the size of the probe (which typically is at least 1.5 mm diameter) causes blurring of the image, leading to difficulties in determining the precise location of edges. Image processing techniques, investigated in Chapter 5, can provide a certain degree of improvement in determinig edge locations, especially for simple geometries, like flat bottomed holes. Nevertheless, we can conclude that the method works well for usual scan conditions, characterized by slowly varying part geometries even with typical commercial probes.

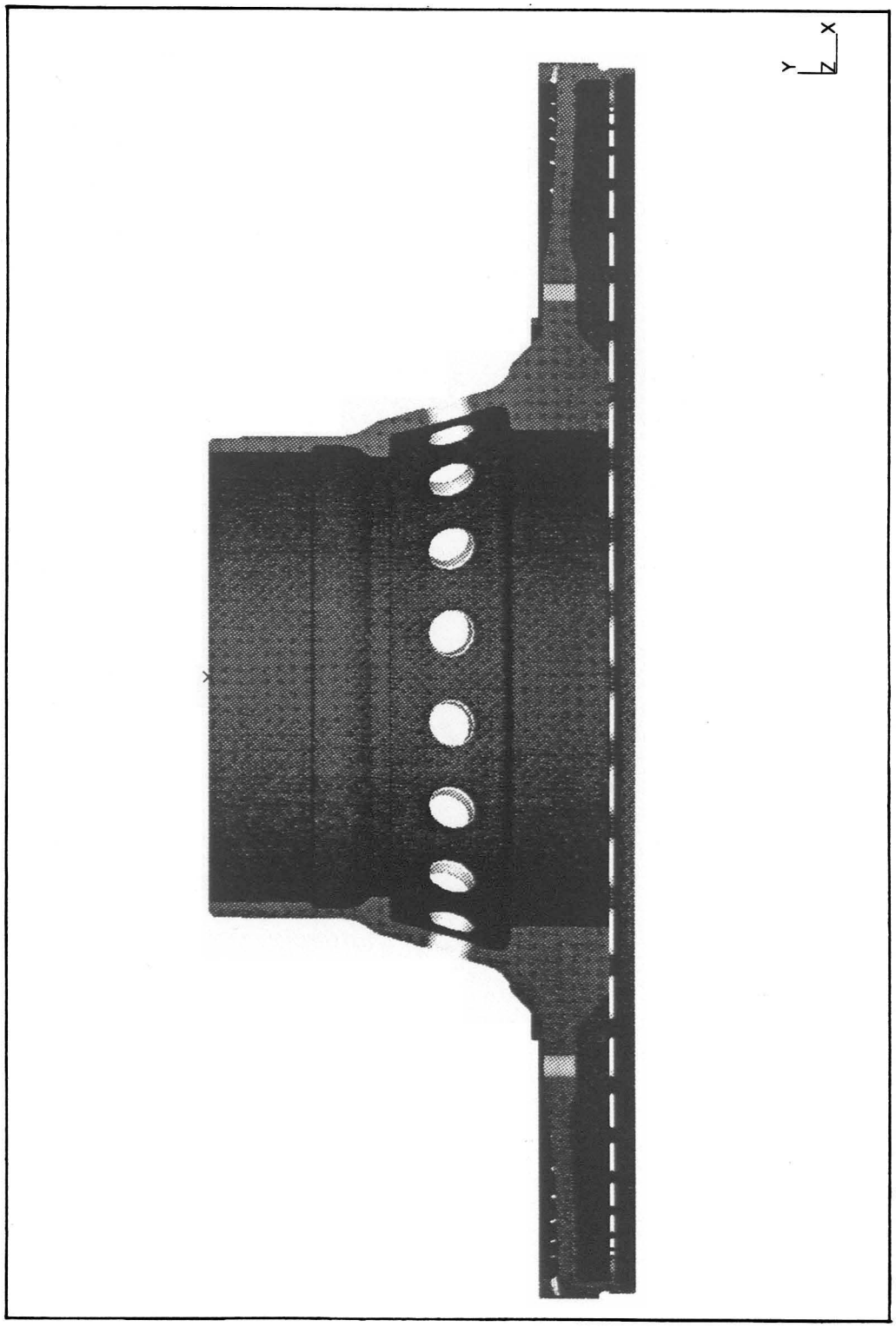

Figure 7.1: Cross section through a turbine disk

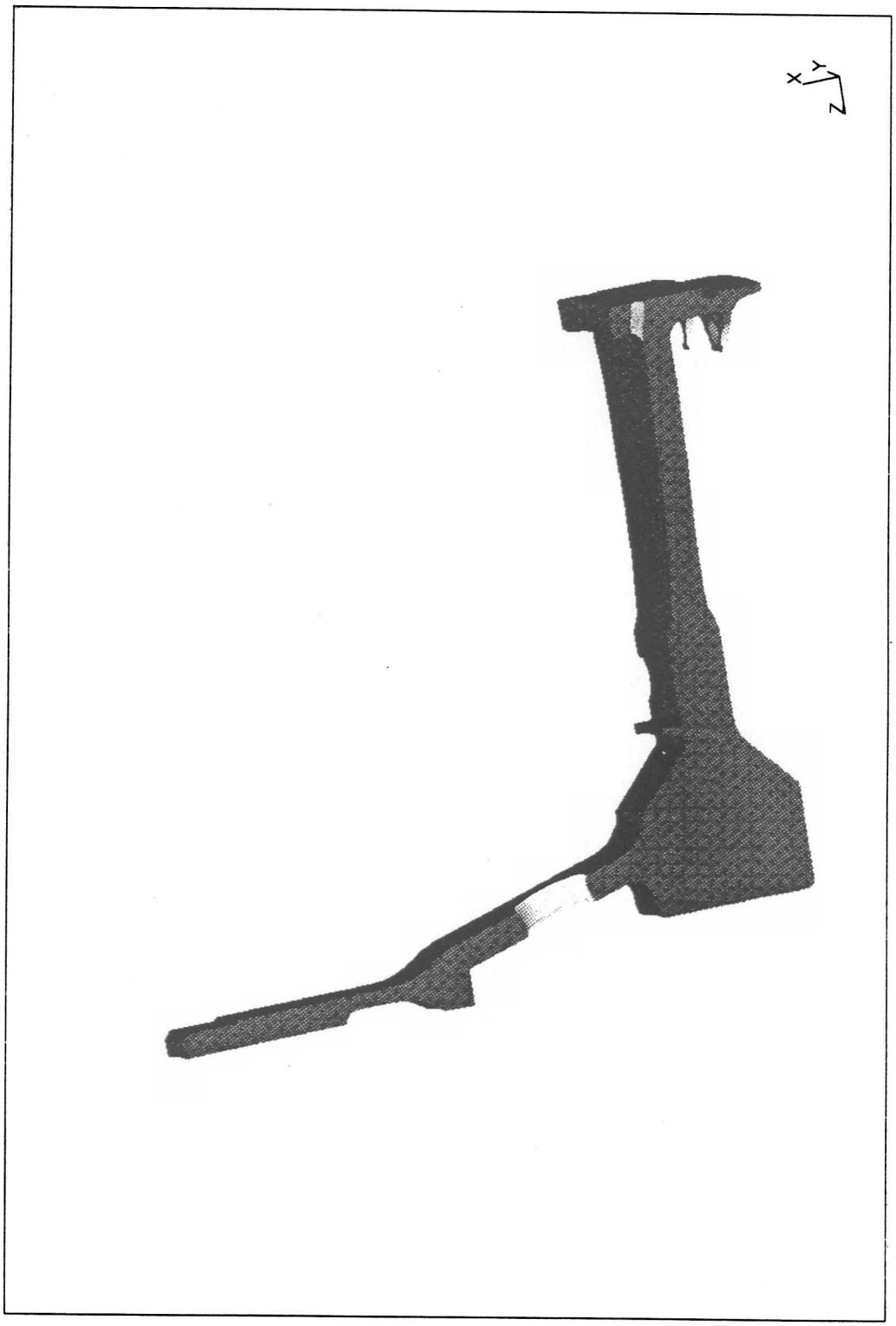

Figure 7.2: Web sector of the turbine disk

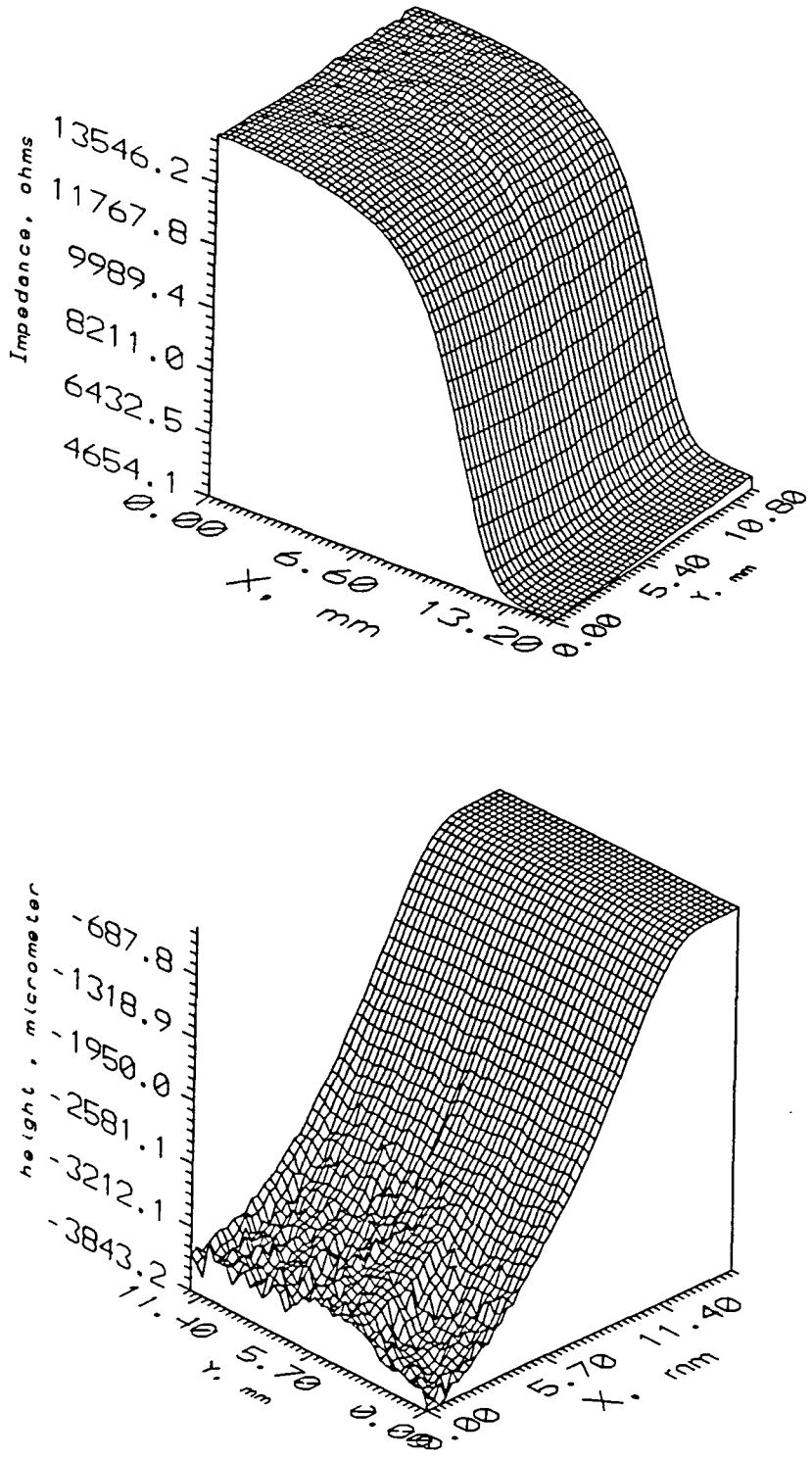

Figure 7.3: Impedance and height map of a scanned area on the web of the turbine disk

7.3 Algorithm for Guiding Sensors in Following Surface Profiles

The ultimate goal of this thesis is to use the sensor output to actively monitor the lift-off of the probe during scanning. For this purpose a new routine was added to the testbed program, which uses a previously determined calibration function to translate impedance data captured by the impedance analyzer into lift-off information. This routine compares at each scan point the user-defined lift-off reference with the calculated lift-off information and moves the probe accordingly along the z axis in order to maintain a constant lift-off for the entire scan. Along each row, the routine keeps track of all previously determined height adjustments in order to estimate the movement required to return the probe to the starting point of the next row. Historical information is also needed to determine the safe height for the probe to return to the starting point. Figure 7.4 describes the main operations performed by the algorithm.

Although the automatic lift-off compensation algorithm results in a reduction in the scan speed, the primary bottleneck in the measurement system is the impedance analyzer. The impedance analyzer is usually programmed to spend at least 0.5 msec (SHORT integration time and averaging factor of 1) for each scan point. In addition to the integration time and averaging factor, another critical parameter which affects scan speed is the step size of probe motion. However, all these factors have a strong effect not only on the speed of the scan, but also on the precision of the lift-off compensation. Based on several series of trials, the best trade-off between speed and precision was obtained when the step size was 0.1 mm, averaging factor of 16 and the integration time is programmed to be SHORT. Figure 7.5 shows the lift-off map obtained from a scan that follows the surface at a 1 mm user-defined reference height

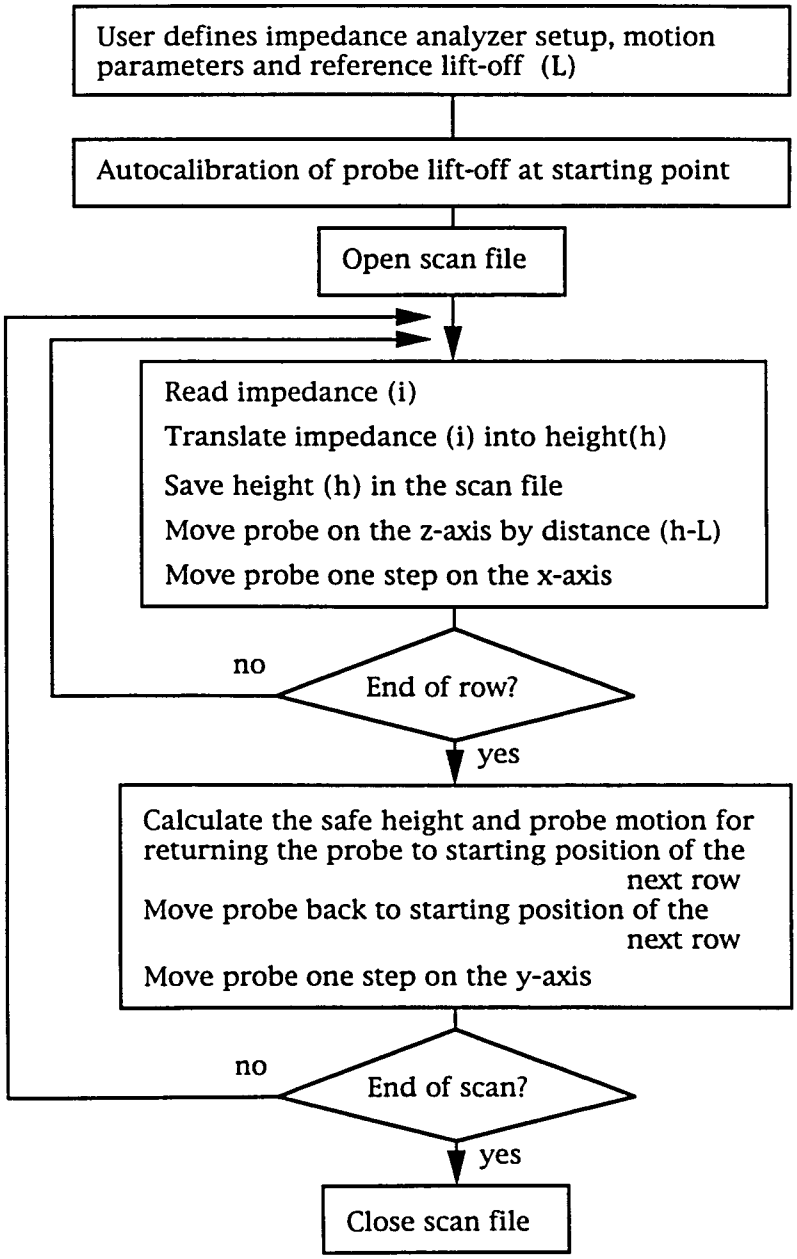

Figure 7.4: Algorithm for guiding sensor to follow a non-planar surface with slow variations

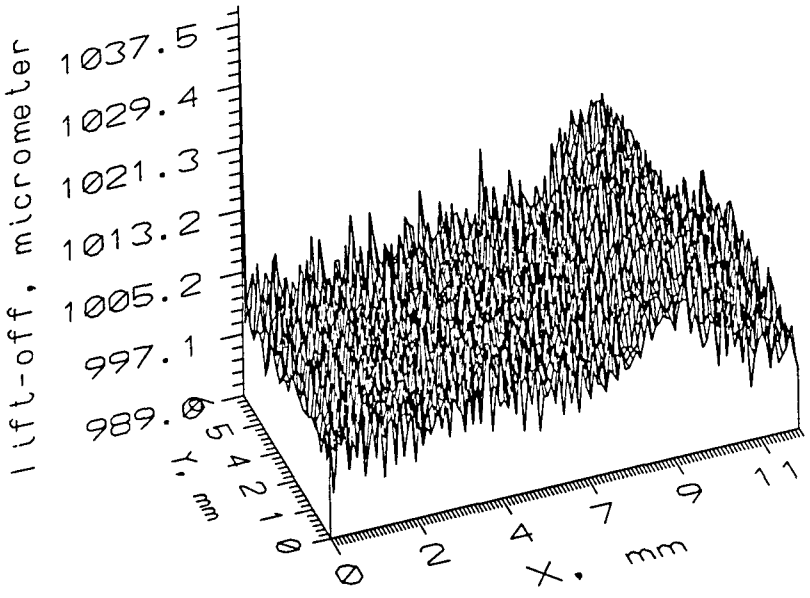

Figure 7.5: Lift-off variations in a surface sensing scan

employing the above-mentioned parameters. It can be seen that lift-off variations in this case are less than 20 micrometers (2% of the reference), and the larger variations are caused by the sharp changes in height. It is, therefore, clear that slowly varying part geometries are more suited for the inductive sensor method.

7.4 Suggestions for Future Work

In order to scan the surface of a complex specimen, the control software uses known information about surface geometry. Information about the surface geometry is usually incorporated in a scan plan file. A scan plan can have a major impact on such factors as the probability of detection (POD). Eddy current inspection requires

particularly accurate scan plan generation because of its sensitivity to probe lift-off variations.

In the past the approach relied primarily on generating scan plans from the CAD drawing of the specimen. The CAD drawings are usually supplied by the manufacturer. The profile information of the object was tested to ensure that all points on the part were accessible to the probe during the scan, and that the probe could be positioned perpendicular to the surface at all times. A program on the DEC workstation performs this verification and generates a suitable scan plan file in terms of the measurement coordinates. The control program then translates this file into commands to control the stepper-motor controllers. This approach has been applied with fairly good results to the pin geometry. However, the main drawbacks of this method are the lack of an automated procedure to ensure that the part matches the design drawing. The method also fails to provide an optimal starting point for the scan. The method also requires a lot of effort to regenerate a scan plan when the geometry is changed. Because the probe is scanned in contact with surface, the method also requires a complicated probe holder.

At the Center for NDE efforts in new directions for generating accurate and flexible scan plans are under way. One of the more recent endeavors is involved in developing a computer-based tool for assisting scan plan generation. Recognizing the mechanical similarity between automated eddy current scan plans and numerically controlled machining, a commercially available CAM software package (MasterCAM) has been adopted for generating the scan plan interactively. The work presented in this thesis complements the above-mentioned effort by providing the necessary feedback for probe path generation. A possible approach would be to prescan the

surface before generating the scan plan formally. The prescan would use the algorithm described in this thesis to follow the surface and would generate a lift-off compensation scan plan file. This procedure would help eliminate problems with manufacturing deviations in the tested sample relative to design drawings. In addition, potential damage to the eddy current probe during scanning can be avoided by constantly providing proximity information.

Another difficult issue in eddy current inspection is the problem of registration. The problem may be caused by manufacturing deviations in the tested sample from its initial design drawing or by any displacement in the use of scan plans on the specimen surface. Before starting a scan, the inspector has to match the scan plan with the corresponding area on the sample and to position the probe at its starting point. This is usually performed by visual inspection or by some rough measurements. Scan tests on pin geometries show the critical nature of this problem. Figure 7.6 presents images of three scans performed on the same curved region of a pin. While the first image shows a scan plot with the correct scan plan and starting point, the other two show scan plots when the starting point is displaced by 0.35 mm along the y axis to the right and to the left, respectively. It can be seen that such small displacements can cause artifacts that can mask the presence of a flaw. In order to avoid starting point displacements, inductive sensor information may be used. The data obtained by proximity sensing in the area of interest may provide sufficient information to locate the starting point with good precision.

In order to obtain better performance in scanning surfaces with sharp changes in height, future work will also have to include development of more complex sensors, such as arrays of inductive or capacitive sensors.

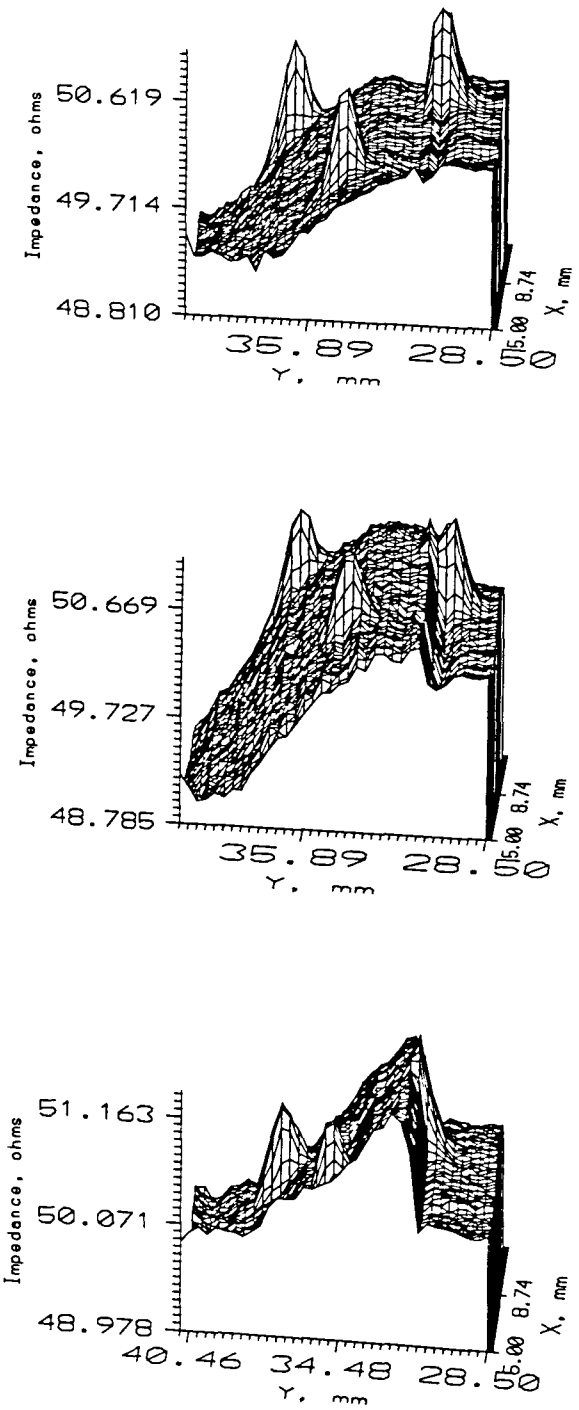

Figure 7.6: Registration problem in pin geometry scans

CHAPTER 8. SUMMARY AND CONCLUSIONS

Eddy current probes are highly sensitive to changes in the distance from the specimen surface, and special techniques must be used to suppress contributions to the signal due to lift-off variations when metal parts are scanned. This is particularly true when parts with complex shapes are inspected, where it becomes critical to control the lift-off of the probe very accurately as the scan is performed. Standard scanning approaches rely on mechanical techniques of spring loading the probe and scanning it in contact with the surface of the part. This approach, however, causes a lot of difficulties and can potentially damage the probe. In order to ensure a reliable and repeatable scan, as well as fast inspection, it is desirable to scan the specimen without contacting the surface and operating at a fixed lift-off. But in this case, other problems can occur: small variations in the surface topography can introduce noise, obscuring flaw signals and reducing the probability of detection (POD). To avoid these problems, the possibility of using eddy current sensors to measure the lift-off distance of the probe, and thereby to map the topography of the surface very accurately has been investigated in this thesis. The final goal is to use the sensor output to actively control the height of the probe, relative to the specimen surface, during scanning.

As experiments show, absolute ferrite-core probes give very good results in moni-

toring lift-off. Three different eddy current probes of this type were tested at different frequencies and on different metal samples to determine their response to changes in height. To aid in the interpretation of these results, a comparison between Dodd and Deeds analytical model and measured data was performed. The agreement obtained emphasizes the need for accurate quantitative measurement systems in order to use inductive sensors with confidence. The best of the three probes was then used to scan a test sample containing a number of surface features including a series of rectangular steps, a gradual incline, and a circular indentation of fixed depth. The probe was scanned over the surface at a fixed height, obtaining an impedance map of the surface. A calibration curve fit using orthogonal polynomials was then used to transform this impedance map into a map of the specimen surface topography. Since the size of the probe causes blurring of the image, image processing techniques were used to improve the resolution of the sensor. Using different edge detection techniques, edge locations were determined with satisfactory results, especially for simple geometries, like flat bottomed holes. Next, the inductive sensor method was applied to a more complex, "real-world" specimen, a turbine engine disk. A program was developed to automatically follow the surface using the inferred height information. Lift-off variations in this case could be reduced up to 2%, without affecting the scan speed too much.

Experiments performed on the test sample as well as on the turbine disk show that inductive sensors can be used with good accuracy for a range of lift-off distances up to 2.5 mm, and the sensitivity of the probe is such that variations as small as a few micrometers can be determined with good precision. Since the calibration curve saturates severely for lift-off distances over 2.5-3 mm, the use of inductive sensors

should be limited to below this range. Another limitation of this method is that the size of the probe (which typically is at least 1.5 mm in diameter) blurs the image, leading to difficulties in determining the precise location of edges. In addition to spatial domain methods investigated in this thesis as image processing techniques, frequency domain methods may be considered. Despite these limitations, we can conclude that the method works well for ordinary scan conditions, characterized by slowly varying part geometries and by typical commercial probes.

As Chapter 7 shows, inductive sensors may be used in various applications of eddy current inspection. Suggestions for future work include:

* use of sensor feedback for probe path generation

* development of algorithms for solving registration problems

* generation of lift-off compensation scan plans.

BIBLIOGRAPHY

[1] Kraus J. D. and Carver K. R., *Electromagnetics*, McGraw-Hill, New York, 1973.

[2] Stucky P. A., "Diffusion Effects in Eddy Current Nondestructive Evaluation," M.S. Thesis, Iowa State University, Ames, 1991.

[3] Halmshaw R., *Non-destructive Testing*, Edward Arnold (Publishers) Ltd., London, 1987.

[4] Dodd C. V., "Solutions to Electromagnetic Induction Problems," Ph.D. Dissertation, University of Tennessee, Knoxville, 1967.

[5] Burrows M. L., "A Theory of Eddy Current Flaw Detection," Ph.D. Dissertation, University of Michigan, Ann Arbor, 1964.

[6] Dodd C. V. and Deeds W. E., "Analytical Solutions to Eddy Current Probe Coil Problems," *J. Appl. Phys.*, 39, 1968, p 2829.

[7] Auld A., Muennemann F. G., and Riaziat M., "Quantitative Modeling of Flaw Responses in Eddy Current Testing," *Research Techniques in Nondestructive Testing*, 7, 1984, p 37.

[8] Moulder J. C., Shull P. J., and Capobianco T. E., "Uniform Field Eddy Current Probe: Experiments and Inversion for Realistic Flaws," *Review of Progress in Quantitative NDE*, 6, 1987, p 601.

[9] Smith E., "Application of Uniform Field Eddy Current Technique to 3-D EDM Notches and Fatigue Cracks," *Review of Progress in Quantitative NDE*, 5A, 1986, p 177.

[10] French P. C., "Eddy Current in a Rectangular Toroid," *IEEE Proc.*, A134, 1987, p 309.

[11] Kahn A. H., Spal R., and Feldman A., "Eddy Current Losses due to a Surface Crack in Conducting Material," *J. Appl. Phys.*, 48, 1977, p 4454.

[12] Lawrenson P. J. and Ralph M. C., "General Three-dimensional Solution of Eddy Current and Laplacian Fields in Cylindrical Structures," *IEEE Proc.*, 117, 1970, p 467.

[13] Bird J. F., "Electromagnetic Induction in Finite-length Cylinders: An Exact Solution," *IEEE Proc.*, A134, 1987, p 761.

[14] Dunbar W. S., "The Volume Integral Method of Eddy Current Modeling," *J. Nondestr. Eval.*, 5, 1985, p 9.

[15] Dunbar W. S., "The Volume Integral Method of Eddy Current Modeling: Verification," *J. Nondestr. Eval.*, 7, 1988, p 43.

[16] Muller W. and Knoblauch A., "A Method for the Calculation of Three-dimensional Eddy Current," *IEEE Trans. Magnet.*, MAG-21, 1985, p 2217.

[17] Hwang J. H. and Lord W., "Finite Element Modeling Of Magnetic Field/Defect Interactions," *ASMT Journal of Testing and Evaluation*, 3, 1975, p 21.

[18] Hwang J. H. and Lord W., "Magnetic Leakage Field Signatures of Material Discontinuities," *Proceedings of the Tenth Symposium on NDE*, San Antonio, April 1975.

[19] Yen W. C., "Finite Element Characterization of Residual Leakage Fields," M.S. Thesis, Colorado State University, Ft. Collins, 1978.

[20] Udpa S. S. and Lord W., "Finite Element Modeling of Residual Magnetic Phenomenon," *International Magnetics Conference*, Boston, April 1980.

[21] Lord W. and Palanisamy R., "Development of Theoretical Models for NDT Eddy Current Phenomena," *Eddy Current Characterization of Materials and Structures*, ASTM STP 722, Birnbaum and Free G., Eds., American Society for Testing and Materials, Philadelphia, 1981.

[22] Palanisamy R. and Lord W., "Finite Element Modeling of Electromagnetic NDT Phenomena," *IEEE Transactions on Magnetics*, MAG-16, No. 5, 1980, p 1083.

[23] Ida N., "Three Dimensional Finite Element Modeling of Electromagnetic NDT Phenomena," Ph.D Dissertation, Colorado State University, Ft. Collins, 1983.

[24] Ida N. and Lord W., "3-D Finite Element Prediction of Magnetostatic Leakage Fields," *IEEE Transactions on Magnetics*, September 1983, p 2260.

[25] Beissner R. E., "Scalar Potential Model of Eddy Current Interactions with Three-dimensional flaws," *J. Nondestr. Eval.*, 7, 1988, p 15.

[26] Banerjee P. K. and Butterfield R., *Boundary Element Methods in Engineering Science*, McGraw-Hill, New York, 1981.

[27] Beissner R. E., Bartels K. A., and Fisher J. L., "Prediction of the Probability of Eddy Current Flaw Detection," *Review of Progress in Quantitative NDE*, 7B, 1988, p 1753.

[28] Gray J. N., Gray T. A., Nakagawa N., and Thompson R. B., "Models for Predicting NDE Reliability," *Metals Handbook*, 17, 1989, p 702.

[29] Bahr A. J. and Cooley D. W., "Analysis and Design of Eddy Current Measurement Systems," *Review of Progress in Quantitative NDE*, 2A, 1983, p 225.

[30] Auld B. A., Jefferies S. R., and Moulder J. C., "Eddy-Current Signal Analysis and Inversion for Semielliptical Surface Cracks," *J. Nondestr. Eval.*, 7, 1988, p 79.

[31] Shull P. J., Moulder J. C., Heyliger P. R., Gimple M., and Auld B. A., "Applications of Capacitive Array Sensors to Nondestructive Evaluation," *Review of Progress in Quantitative NDE*, 7A, 1988, p 517.

[32] Capobianco T. E., and Ciciora S. J., "Characterizing Differential Air-core Eddy Current Probes," *Review of Progress in Quantitative NDE*, 10A, 1991, p 897.

[33] Rosengreen A., Bahr A. J., and Marsland D. M., "Inductive Arrays for Near-field Edge Tracking and Ranging," *Review of Progress in Quantitative NDE*, 7A, 1988, p 493.

[34] Moulder J. C. et al., "Calibration Methods for Eddy Current Measurement Systems," *Review of Progress in Quantitative NDE*, 4A, 1985, p 411.

[35] Press W. H. et al., *Numerical Recipes in C - The Art of Scientific Computing*, Cambridge University Press, New York, 1988.

[36] Ralston A. and Rabinowitz A., *A First Course in Numerical Analysis*, 2nd edition, McGraw-Hill, New York, 1978.

[37] McCary R. O. et al., "Eddy Current Imaging," *IEEE Transactions on Magnetics*, Mag-20, 1984, p 1986.

[38] Gonzalez R. C. and Woods R. E., *Digital Image Processing*, Addison-Wesley Inc., Reading, Massachusetts, 1992.

[39] Jain A. K., *Fundamentals of Digital Image Processing*, Prentice-Hall Inc., Englewood Cliffs, New Jersey, 1989.